NeuroImage 254 (2022) 119137

Contents lists available at ScienceDirect

NeuroImage

journal homepage: www.elsevier.com/locate/neuroimage

In vivo Correlation Tensor MRI reveals microscopic kurtosis in the human brain on a clinical 3T scanner

Lisa Novello[a,1,*], Rafael Neto Henriques[b,1,*], Andrada Ianuş[b], Thorsten Feiweier[c], Noam Shemesh[b,2], Jorge Jovicich[a,2]

[a] *Center for Mind/Brain Sciences - CIMeC, University of Trento, Rovereto, Italy*
[b] *Champalimaud Research, Champalimaud Foundation, Lisbon, Portugal*
[c] *Siemens Healthcare GmbH, Erlangen, Germany*

ARTICLE INFO

Keywords:
Double-diffusion encoding
Kurtosis
Non-Gaussian diffusion
Human brain
Magnetic resonance imaging
Correlation tensor MRI

ABSTRACT

Diffusion MRI (dMRI) has become one of the most important imaging modalities for noninvasively probing tissue microstructure. Diffusional Kurtosis MRI (DKI) quantifies the degree of non-Gaussian diffusion, which in turn has been shown to increase sensitivity towards, *e.g.*, disease and orientation mapping in neural tissue. However, the specificity of DKI is limited as different sources can contribute to the total intravoxel diffusional kurtosis, including: variance in diffusion tensor magnitudes (K_{iso}), variance due to diffusion anisotropy (K_{aniso}), and microscopic kurtosis (μK) related to restricted diffusion, microstructural disorder, and/or exchange. Interestingly, μK is typically ignored in diffusion MRI signal modelling as it is assumed to be negligible in neural tissues. However, recently, Correlation Tensor MRI (CTI) based on Double-Diffusion-Encoding (DDE) was introduced for kurtosis source separation, revealing non negligible μK in preclinical imaging. Here, we implemented CTI for the first time on a clinical 3T scanner and investigated the sources of total kurtosis in healthy subjects. A robust framework for kurtosis source separation in humans is introduced, followed by estimation of μK (and the other kurtosis sources) in the healthy brain. Using this clinical CTI approach, we find that μK significantly contributes to total diffusional kurtosis both in grey and white matter tissue but, as expected, not in the ventricles. The first μK maps of the human brain are presented, revealing that the spatial distribution of μK provides a unique source of contrast, appearing different from isotropic and anisotropic kurtosis counterparts. Moreover, group average templates of these kurtosis sources have been generated for the first time, which corroborated our findings at the underlying individual-level maps. We further show that the common practice of ignoring μK and assuming the multiple Gaussian component approximation for kurtosis source estimation introduces significant bias in the estimation of other kurtosis sources and, perhaps even worse, compromises their interpretation. Finally, a twofold acceleration of CTI is discussed in the context of potential future clinical applications. We conclude that CTI has much potential for future *in vivo* microstructural characterizations in healthy and pathological tissue.

1. Introduction

Mapping microstructural features of the brain, *in vivo* and non-invasively, has been a central endeavour of the MRI community for more than three decades. Diffusion-weighted MRI (dMRI) has played a key role in such microstructural characterizations due to its ability to sensitize the MRI signal towards diffusion-driven molecular displacements, which then "sense" tissue boundaries in the range of around >10 μm (in typical clinical settings). Water molecules are highly abundant in tissues and can traverse several micrometers in a typical MR-relevant diffusion time, making dMRI an excellent indicator of tissue microstructure. At relatively low diffusion weighting, the unidirectional Apparent Diffusion Coefficient (ADC, Stejskal and Tanner, 1965; Le Bihan et al., 1986) and later the rotationally invariant Diffusion Tensor Imaging approaches (DTI, Basser et al., 1994) utilized a Gaussian diffusion framework for quantifying diffusivities, which found numerous applications from stroke detection, to white matter orientation mapping, to characterizing progressive changes in brain tissue due to plasticity (*e.g.* Moseley et al., 1990; Gauvin et al., 2001; Anwander et al., 2007; Roebroeck et al., 2008; Della-Maggiore et al., 2009; Scholz et al., 2009; Blumenfeld-Katzir et al., 2011; McNab et al., 2013a; Baron et al., 2015; Benetti et al., 2018; Hasan et al., 2018; Jacobacci et al., 2020, Yon et al., 2020,

* Corresponding authors.
E-mail addresses: lisa.novello@unitn.it (L. Novello), rafael.henriques@neuro.fchampalimaud.org (R.N. Henriques).
[1] These authors contributed equally to this work.
[2] These authors contributed equally to this work as last authors.

https://doi.org/10.1016/j.neuroimage.2022.119137.
Received 4 November 2021; Received in revised form 17 February 2022; Accepted 22 March 2022
Available online 23 March 2022.
1053-8119/© 2022 The Authors. Published by Elsevier Inc. This is an open access article under the CC BY license (http://creativecommons.org/licenses/by/4.0/)

for a review see *e.g.* Mukherjee, 2005; Assaf and Pasternak, 2008; Johansen-Berg, 2010).

Deviations from Gaussian displacement profiles were described quite early within the framework of q-space MR (Callaghan et al., 1991; Assaf and Cohen, 1998). As high-performance gradient systems became more readily available in clinical MRI settings, a wider range of diffusion-weighting regimes could be probed, providing evidence for non-Gaussian signal decay in q-space experiments also in the human brain (Mulkern et al., 1999). Since q-space gradients required very high diffusion weighting and require attenuation of the signal up to the noise floor, a general methodology for characterizing diffusion weighted signals at an intermediate diffusion weighting regime was elegantly introduced by Jensen et al. (2005) and Jensen and Helpern (2010). The ensuing Diffusion Kurtosis Imaging (DKI) methodology is a "signal representation" approach (Novikov et al., 2018; Novikov, 2021, as opposed, *e.g.*, to microstructural models, for instance: Jespersen et al., 2007; Fieremans et al., 2011; Zhang et al., 2012; Kaden et al., 2016; Jespersen, 2018) based on the cumulant expansion of the dMRI signal up to the second order in b-value (with $b = \gamma^2\delta^2G^2(\Delta - \delta/3)$ for ideal rectangular diffusion-sensitizing gradients, where γ is the gyromagnetic ratio, δ is the gradient pulse duration, Δ is the separation between the two leading edges of the gradient pulses, and G is the gradient pulse's magnitude). DKI quantifies the excess-kurtosis in water displacement probability which can be used as an index of diffusion non-Gaussianity, which presumably reflects the heterogeneity of the diffusion process in tissue microstructure (Jensen et al., 2005; Jensen and Helpern, 2010; Wu and Cheung, 2010). DKI has been successfully adopted to study both the healthy and the diseased human brain, providing insights into individual anatomical details at high resolution (Mohammadi et al., 2015), development (Huber et al., 2019), ageing (Falangola et al., 2008; Henriques, 2018), attention deficit hyperactivity disorder (ADHD, Helpern et al., 2011), neurodegenerative disorders (Arab et al., 2018) such as Alzheimer's (Gong et al., 2013; Struyfs et al., 2015) and Parkinson's disease (Wang et al., 2011; Kamagata et al., 2013, 2014; Surova et al., 2018), and brain tumors (Raab et al., 2010; Raja et al., 2016; Delgado et al., 2018; Hempel et al., 2017, 2018; Lin et al., 2018). Indeed, DKI is nowadays implemented on many different imaging platforms (*e.g.* Leemans et al., 2009; Tabesh et al., 2011; Tournier et al., 2019; Henriques et al., 2021a).

By imparting higher b-values, DKI can potentially provide more information on the tissue's diffusion profile than its DTI counterpart (*e.g.* Falangola et al., 2008; Wang et al., 2011; Hui et al., 2012; Zhuo et al., 2012; Fieremans et al., 2013; Steven et al., 2014; Lin et al., 2018). However, at the same time, DKI lacks specificity because many different factors can contribute to non-zero excess kurtosis. At the voxel level, diffusion kurtosis may arise from mesoscopic effects such as the orientation dispersion of fibers and their specific configuration (Lu et al., 2006; Henriques et al., 2015). At the microscopic level (*i.e.* (sub)cellular level, or more generally at the level of pores or microdomains, where a microdomain can be defined as a uniform subvoxel segment, Szczepankiewicz et al., 2015), diffusion kurtosis may arise from different sources, including the following (Jespersen et al., 2019; Henriques et al., 2020, 2021c):

(i) Kurtosis arising from variance of the eigenvalues of individual diffusion tensors representing tissue microdomains, thus arising from *diffusion tensor shape* variance (*i.e.* deviations of the shape of pores or microdomains from a sphere), which is referred to as anisotropic kurtosis (K_{aniso}).

(ii) Kurtosis associated with the variance in diffusion tensor magnitudes across the ensemble of all microdomains, thus arising from *diffusion tensor size* variance, which is referred to as isotropic kurtosis (K_{iso}; the subscript "iso" here refers to the isotropic part of the tensor (its magnitude), and does not require any of the tensors to have identical eigenvalues).

(iii) Kurtosis associated with non-Gaussian diffusion effects within restricting "pores" (restricted diffusion, Callaghan et al., 1991), within complex structures in which diffusion effects are not completely coarse grained (Novikov et al., 2014, 2019; Fieremans et al., 2016; Lee et al., 2020a), or a combination of restriction and exchange in exchanging components (Olesen et al., 2022), both of which are referred to as microscopic kurtosis (μK, also previously called intra-compartmental kurtosis, K_{intra}, in Jespersen et al., 2019; Henriques et al., 2020; Henriques et al., 2021b).

Understanding how each of these different sources affect the kurtosis signal can be challenging. DKI, and, more generally, techniques based on Single Diffusion Encoding sequences (SDE, Shemesh et al., 2016) with moderate b-values cannot resolve the relative contribution of each source without making strong assumptions about tissue properties (Fieremans et al., 2011; Ianuş et al., 2016). Such assumptions, however, may confound the specificity of the derived estimates (Jelescu et al., 2015; Lampinen et al., 2017; Henriques et al., 2019), leading to potential serious errors in the "microstructural" interpretation of the metrics (Jelescu et al., 2016; Novikov et al., 2018).

Nevertheless, resolving each diffusion kurtosis source has the potential of unravelling important microstructural information that can provide new insights into tissue properties which, in turn, may have clinical impact (Szczepankiewicz et al., 2015, 2016; Nilsson et al., 2020; Alves et al., 2022). For this reason, Multidimensional Diffusion Encoding (MDE, Eriksson et al., 2013; Lasič et al., 2014; Westin et al., 2016; Shemesh et al., 2016; Topgaard, 2017) methods have been developed to produce richer diffusion weighting paradigms allowing to explore correlations between different spatial dimensions, and, ultimately, to yield more specific tissue contrasts. Among MDE preparations, Double Diffusion Encoding (DDE, Mitra, 1995; Shemesh et al., 2010a, 2016, Henriques et al., 2021b) in the long mixing time regime has been used in combination with either trapezoidal or oscillating gradients (Double Oscillating Diffusion Encoding, DODE, Ianuş et al., 2017; Shemesh, 2018), and with metabolites spectroscopy to probe the displacements of specific metabolites (DDE MRS, Shemesh et al., 2014, 2017; Vincent et al., 2020; Lundell et al., 2021). Such applications stemmed from the initial theoretical work (Mitra, 1995; Cheng and Cory, 1999; Özarslan and Basser, 2008; Özarslan, 2009; Lawrenz et al., 2010; Jespersen and Buhl, 2011; Jespersen, 2012) and the following experimental observations confirming that DDE provides signal differences for collinear and orthogonal diffusion gradients in locally anisotropic samples with overall random orientation (Cheng and Cory, 1999; Callaghan and Komlosh, 2002) and angular modulations of the signal in the presence of pores characterized by eccentricity over the plane sampled by the diffusion preparation (Shemesh et al., 2010a, 2010b, 2011; Shemesh et al., 2012a). Since then, DDE in the long mixing time regime has been extensively adopted to provide different parameters associated with microscopic diffusion anisotropy (a quantity related to K_{aniso}, see methods) which reports on the anisotropy of the tissue at the pore or microdomain length scale independently to confounding orientation dispersion effects (*e.g.* Jespersen et al., 2013; Lasič et al., 2014; Shemesh et al., 2016; Ianuş et al., 2018; Henriques et al., 2020). Microscopic diffusion anisotropy has been investigated using DDE in preclinical systems in both white and grey matter, *e.g.*: in fixed grey matter (Komlosh et al., 2007), pig spinal cord (Komlosh et al., 2008), pig optic nerve and cortical grey matter, with phantoms mimicking their respective microstructures (Shemesh et al., 2010b, 2011; Shemesh and Cohen, 2011; Shemesh et al., 2012a), in both *in vivo* and *ex vivo* rat brain (Shemesh et al., 2012b; Ianuş et al., 2018; Kerkelä et al., 2019), in *ex vivo* monkey brain (Jespersen et al., 2013), in rat spinal cord injury (Budde et al., 2017), and in *ex vivo* rat spinal cord (Shemesh, 2018). In clinical systems DDE microscopic diffusion anisotropy estimates have been reported in pig spinal cord (Lawrenz and Finsterbusch, 2011), and successfully mapped in the *in vivo* healthy human brain white matter

(Lawrenz and Finsterbusch, 2013, 2015), cortical grey matter (Lawrenz and Finsterbusch, 2019), in the study of ageing (Lawrenz et al., 2016), and in clinical applications, where it showed increased specificity compared to DTI-derived FA in multiple sclerosis lesions (Yang et al., 2018) and has been investigated in Parkinson's disease (Kamiya et al., 2020).

In addition to DDE preparations, alternative MDE pulse sequences have been adopted in parallel with the aim of resolving the kurtosis sources: previous studies showed that, under the strict Multiple Gaussian Component assumption (MGC), tensor-valued information of MDE sequences can decompose K_t as the sum of K_{aniso} and K_{iso} (Szczepankiewicz et al., 2015, 2019a; Topgaard, 2019). These techniques have been successfully adopted in the study of healthy brain microstructure (Lampinen et al., 2019, 2020a; Tax et al., 2020), for improving the estimation of different microstructural models (Topgaard, 2017; Coelho et al., 2019; Cottaar et al., 2020), and demonstrated great promise for clinical utility (Szczepankiewicz et al., 2015, 2016; Lampinen et al., 2020b; Winther Andersen et al., 2020) and implementation (Szczepankiewicz et al., 2019a; Nilsson et al., 2020, 2021). These so-called "tensor-valued" approaches, however, assume that all underlying diffusion propagators within the voxel can be approximated as multiple Gaussian components, with negligible μK and negligible time dependence (Jespersen et al., 2019) and thus cannot be used to map kurtosis sources not considered by this picture, such as the kurtosis related to the non-Gaussian diffusion effects of restricted diffusion, incomplete coarse-graining, and exchange, *i.e.* the microscopic kurtosis sources referred above (Jespersen et al., 2019; Henriques et al., 2020, 2021c; Paulsen et al., 2015; Olesen et al., 2022; Alves et al., 2022).

Recently, a new DDE strategy has been proposed to provide a more complete separation of different kurtosis sources, namely the Correlation Tensor Imaging, or CTI (Henriques et al., 2020; Henriques et al., 2021c). In particular, CTI enables the simultaneous estimation of K_{iso}, K_{aniso}, and μK, by relying on the acquisition of four different DDE sets (*i.e.* combinations of gradient waveforms comprising four unique amplitudes and direction combinations) and on the cumulant expansion of DDE signals at long mixing times. So far, the CTI methodology has been applied in both *in vivo* and *ex vivo* rodent brains (Henriques et al., 2020; Henriques et al., 2021c; Alves et al., 2022), revealing the expected contrasts for K_{aniso}, the dominant kurtosis source in white matter, as well as the expected contrasts for K_{iso}, which highlights areas with large dispersion of microdomains' mean diffusivities such as regions with partial volume effects. However, crucially, these first CTI data, both *ex vivo* and *in vivo*, unequivocally demonstrated evidence of a positive non-vanishing μK both in rodent white and grey matter, with μK being the dominant kurtosis source in grey matter (Henriques et al., 2021c). Further CTI experiments in a rodent stroke model strongly suggested a potential role for μK as an important new biomarker and suggested that cytotoxic and other types of edema could potentially be resolved via CTI (Alves et al., 2022). Together with the observation of biases in K_{aniso} and K_{iso} when not accounting for μK in mice (Henriques et al., 2021c), this body of evidence prompts the translation of the CTI methodology to the clinical setting, building also on previous successful applications of DDE sequences in the study of the living human brain (Lawrenz and Finsterbusch, 2013, 2015, 2019).

In this work, we set out to develop CTI for humans for the first time. Using a clinical 3T system, we investigate the kurtosis sources emerging from a cohort of healthy subjects. In particular, the goals of this study are (i) to evaluate the feasibility of acquiring DDE data adhering to the CTI methodology proposed in Henriques et al. (2021c), in a clinical 3T system; (ii) to estimate the kurtosis sources in brain tissue derived by the CTI framework from healthy adult volunteers, particularly with respect to evaluating evidence for the μK component in humans; and (iii) to investigate the possible implications of ignoring the μK component, as currently established in alternative approaches aiming to resolve kurtosis sources.

2. Materials and methods

2.1. Correlation tensor imaging theory

In the long mixing time regime, when the Z tensor approaches the correlation tensor and Q and S tensors are decoupled from the signal (Jespersen and Buhl, 2011; Jespersen, 2012; Jespersen et al., 2013), the powder average of DDE signals is equivalent to (Henriques et al., 2021c):

$$\begin{aligned} log\left(\bar{E}_{DDE}(b_1,b_2,\theta)\right) = &-(b_1+b_2)\bar{D}+\frac{1}{6}\left(b_1^2+b_2^2\right)\bar{D}^2K_t \\ &+\frac{1}{2}b_1b_2cos^2\theta\bar{D}^2K_{aniso} \\ &+\frac{1}{6}b_1b_2\bar{D}^2\left(2K_{iso}-K_{aniso}\right)+O\left(b^3\right) \end{aligned} \quad (1)$$

where b_1 and b_2 are the b-values of the first and of the second pair of diffusion gradients, respectively, θ is the angle between the directions of the first and the second pair of diffusion gradients, $\bar{D}$ is the mean diffusivity, K_t is the total kurtosis of the powder averaged signal, $K_{aniso} \equiv \frac{6}{5}\frac{\langle \mathrm{var}(\lambda_i)\rangle}{D^2}$ with $\langle \mathrm{var}(\lambda_i)\rangle$ representing the eigenvalue variance of microenvironments averaged across the multiple compartments and D is the mean diffusivity, and $K_{iso} \equiv 3\frac{\mathrm{var}(\langle\lambda_i\rangle)}{\mathrm{D}^2}$ with $\mathrm{var}(\langle\lambda_i\rangle)$ representing the variance across the ensemble of all microdomains' tensor magnitudes (Szczepankiewicz et al., 2016; Henriques et al., 2020). Note that K_{aniso} can be directly related to previous DDE/MDE microscopic diffusion anisotropy measurements: defining the microscopic diffusion anisotropy as $\mu A^2 \equiv \frac{3}{5}\langle \mathrm{var}(\lambda_i)\rangle$ (Shemesh et al., 2016; Ianuş et al., 2018; Henriques et al., 2021b) and pore eccentricity as $\varepsilon \equiv \frac{3\Delta^2}{5}\langle \mathrm{var}(\lambda_i)\rangle$ (Cheng and Cory, 1999; Lawrenz et al., 2011; Jespersen et al., 2013), K_{aniso} can be directly related to these measures by the following expressions $K_{aniso} = 2\mu A^2/D^2$ and $K_{aniso} = 2\varepsilon/\Delta^2D^2$. K_{aniso} can also be converted to microstructural fractional anisotropy (Lasič et al., 2014; Szczepankiewicz et al., 2015) or fractional eccentricity (Jespersen et al., 2013) using the following expressions $\mu FA = \sqrt{\frac{3}{2}K_{aniso}/(K_{aniso}+\frac{6}{5})}$ and $FE = \sqrt{K_{aniso}/(K_{aniso}+\frac{6}{5})}$.

By estimating K_t, K_{aniso}, and K_{iso}, microscopic kurtosis μK can then be extracted by a simple subtraction as follows (Henriques et al., 2020, 2021c):

$$\mu K = K_t - K_{aniso} - K_{iso} \quad (2)$$

Thus, while information on K_t can be accessed by conventional SDE experiments with at least two non-zero b-values, its decomposition in its sources requires the use of DDE preparations. Importantly, as described in Henriques et al. (2021c), the difference between the logarithm of powder averaged signals from an SDE-like set with b-value b_a and a parallel DDE set with the b-value of each pair of gradients being $b_a/2$ can be used to directly access μK as follows:

$$log\left(\bar{E}_{DDE}(b_a,0,0°)\right) - log\left(\bar{E}_{DDE}\left(\frac{b_a}{2},\frac{b_a}{2},0°\right)\right) = \frac{1}{12}b_a^2\bar{D}^2\mu K + O\left(b^3\right) \quad (3)$$

and, in addition, K_{aniso} can be directly estimated from the difference between the logarithm of parallel and perpendicular sets (Jespersen et al., 2013; Ianuş et al., 2018):

$$\begin{aligned} &log\left(\bar{E}_{DDE}\left(\frac{b_a}{2},\frac{b_a}{2},0°\right)\right) - log\left(\bar{E}_{DDE}\left(\frac{b_a}{2},\frac{b_a}{2},90°\right)\right) \\ &= \frac{1}{2}b_a^2\bar{D}^2K_{aniso} + O\left(b^3\right) \end{aligned} \quad (4)$$

with the higher order terms $O(b^3)$ ignored in the current analysis.

2.2. Participants

Ten participants (mean age ± one standard deviation (SD): 28.9 ± 6.0 years, six males) gave informed consent to participate in this study

approved by the Research Ethics Committee of the University of Trento. At the time of MRI scans, all participants were healthy and had no medical history of neurological or psychiatric disorders.

2.3. MRI acquisition

Data were acquired at the center for Mind/Brain Sciences of the University of Trento, Italy, on a 3T clinical MR scanner (MAGNETOM Prisma, Siemens Healthcare, Erlangen, Germany), with a 64-channel head-neck RF receive coil. Head motion during the acquisition was limited using foam paddings optimized for head coils. Anatomical T1-weighted (T1w) Multi-Echo MPRAGE (ME-MPRAGE, van der Kouwe et al., 2008) images were acquired with the following parameters: $TE_1/TE_2/TE_3/TE_4$ = 1.69/3.55/5.41/7.27 ms, TR = 2530 ms, TI = 1100 ms, flip angle: 7°, 1 mm-isotropic resolution, matrix size: 256 × 256.

For the diffusion-weighted data acquisition, a prototype double-spin-echo DDE sequence was used (Fig. 1A). A double-spin-echo sequence (rather than a single-spin-echo sequence with pairs of diffusion gradients on either side of the refocusing pulse) was chosen to mitigate concomitant gradient effects (Callaghan and Komlosh, 2002; Szczepankiewicz et al., 2019c). The DDE sequence imaging parameters were: TR = 5600 ms, TE = 127 ms, matrix size: 84 × 84, slice thickness: 2.5 mm, no slice gap, spatial resolution: 2.5 mm-isotropic, 60 axial slices allowing full brain coverage, partial Fourier factor: 6/8, GRAPPA/SMS factors: 2/4. Four sets of DDE images were acquired according to the optimization described in Henriques et al. (2021c) (Fig. 1B):

- DDE set #1: b_1 = 1000 s/mm^2, b_2 = 0, with b_t = 1000 s/mm^2.
- DDE set #2: b_1 = 2000 s/mm^2, b_2 = 0, with b_t = 2000 s/mm^2.
- DDE set #3: b_1 = 1000 s/mm^2, b_2 = 1000 s/mm^2, with b_t = 2000 s/mm^2 and parallel directions for the first and the second pairs of diffusion gradients ($\theta = 0°$).
- DDE set #4: b_1 = 1000 s/mm^2, b_2 = 1000 s/mm^2, with b_t = 2000 s/mm^2 and perpendicular directions for the first and the second pairs of diffusion gradients ($\theta = 90°$).

In the above equations, b_t is the total b-value considering both the first and the second pairs of diffusion gradients. The b-value for these experiments were selected according to Henriques et al. (2020), which show that a CTI protocol with a maximum b-value between 1500 s/mm^2 and 2000 s/mm^2 provides a good compromise between kurtosis estimation accuracy (minimization of high order effects) and precision (enough contrast to noise for kurtosis estimation). Moreover, the total b-values for DDE #2, #3, and #4 were set to be equal to minimize different high-order-effect of the different acquisition schemes Henriques et al., 2021c). For all DDE sets, $\delta/\Delta/\tau_M$ = 15.8/31.8/32.3 ms. Sixty diffusion-weighted volumes were acquired per each DDE set: for sets #1, #2, and #3 directions from a 3-dimensional 60-point spherical 10-design were used (Hardin and Sloane, 1996), while for set #4, perpendicular directions from the 5-design in Jespersen et al. (2013) were used. For the phantom and all participants, one volume without diffusion gradients (hereafter referred to as "$b = 0''$ volume) was added every 12 diffusion-weighted volumes, and two additional $b = 0$ volumes were acquired at the beginning of set #2 and #4 (except for sub-01 and sub-02 (Fig. 3), where two $b = 0$ volumes were included for each DDE set and TR = 5500 ms was used). Finally, two $b = 0$ volumes with reversed phase encoding were acquired to correct for susceptibility-induced geometric distortions (see *Image processing* section). DDE sets were acquired in the following temporal order to guarantee the possibility of directly estimating μK and K_{aniso} in case of a participant-related acquisition interruption (see Eqs. (3) and (4): DDE set #2, DDE set #3, DDE set #4, DDE set #1. Two repetitions of the above listed sets were acquired, each with opposite polarity of all diffusion gradients (hereafter referred to as "positive" and "negative", Fig. 1B, bottom) to mitigate potential cross-term effects with imaging gradients (Neeman et al., 1991; Lawrenz and Finsterbusch, 2011; Ianuş et al., 2018). The total acquisition time for the two repetitions was around 52 min.

To check for the fulfillment of the long mixing time regime assumption (Shemesh et al., 2012b; Henriques et al., 2020), twelve parallel directions were selected from the gradient scheme for DDE set #3, and the polarity of the direction of the second pair of diffusion gradients was reversed to yield antiparallel gradients (Shemesh et al., 2012b; Henriques et al., 2020). Images corresponding to this subset of parallel and antiparallel gradient directions were acquired twice, each with opposite polarity of the diffusion gradients, followed by ten additional $b = 0$ volumes acquired for assessing the temporal Standard Deviation (tSD) of this series and relate it to the signal difference between parallel and antiparallel images for all participants (except for sub-01 and sub-02).

To verify the absence of systematic imaging artifacts, the above-described protocol was additionally acquired on a brain-sized spherical isotropic phantom at the room temperature of 22 °C, filled with water doped with Nickel Sulphate ($NiSO_4(H_2O)_6$).

2.4. Image processing

Diffusion-weighted images: dMRI data were denoised with the Marchenko-Pastur (MP) PCA denoising in MRtrix v. 3.0.2 (Veraart et al., 2016), and MP PCA-estimated noise variance maps were visually inspected along with denoising residuals. Data were then corrected for Gibbs ringing (Kellner et al., 2016), and the susceptibility-induced field was estimated using $b = 0$ volumes with opposite phase encoding in FSL's *topup* (Andersson et al., 2003). Data corresponding to each set was then corrected for eddy currents and head motion in FSL's *eddy* (Andersson and Sotiropoulos, 2016), by using the first acquired $b = 0$ volumes as reference volume for all sets, to get all the images aligned to the same reference volume. For DDE sets where the amplitude of the second pair of diffusion gradients was not zero (DDE set #3, DDE set #4), the direction of the second pair of diffusion gradients was used in *eddy*, motivated by the observation for a much smaller impact of the first pair of diffusion gradients on eddy currents artifacts (Mueller et al., 2017), and as reported in Yang et al. (2018) and Fan et al. (2020). Summary metrics of the quality of each participant's images were then computed with the *eddy qc* framework (Bastiani et al., 2019). Diffusion-weighted volumes were then concatenated according to their temporal order and corrected for signal drift (Vos et al., 2017) and bias field (Tustison et al., 2010). Phantom images underwent the same pre-processing pipeline adopted for human data. Before computing each participant's (*i.e.* individual) CTI maps, data were smoothed with a 3D Gaussian filter (using a Gaussian kernel with FWHM = 1.25, scipy v. 1.6.1); the FWHM adopted in the smoothing process is in line with values adopted in early DKI studies (*e.g.* Lu et al., 2006; Falangola et al., 2008; Henriques et al., 2015). This smoothing step was applied with the aim of mitigating the effects of potential residual noise on kurtosis estimates manifesting as negative kurtosis values, a phenomenon often observed in DKI analyses which has motivated the use of smoothing in the literature (Henriques et al., 2021d). Furthermore, pairs of images corresponding to opposite polarities of the diffusion gradients were geometrically averaged to mitigate effects associated with potential imaging cross-terms (Neeman et al., 1991; Lawrenz and Finsterbusch, 2011, 2013; Ianuş et al., 2018). Images were then directionally averaged in order to get four powder average (p.a.) images, one per each set, which were finally normalized (hereafter referred to as p.a.$_{norm}$) by the mean of the $b = 0$ volumes included across all the acquired DDE sets (Fig. 2A). SNR maps of $b = 0$ volumes ($SNR_{b=0}$) were computed by dividing the mean($b = 0$) voxel-wise signal by an estimate of the noise represented by the voxel-wise standard deviation across the $b = 0$ acquisitions (tSD) (Fig. 2B). SNR maps of diffusion-weighted volumes were computed by dividing p.a. images by the tSD estimate, per each set (SNR_{PA}-set#N, where N is the number of the considered DDE set) (Table S1). All SNR maps were computed for each subject individually and prior to the application of the smooth-

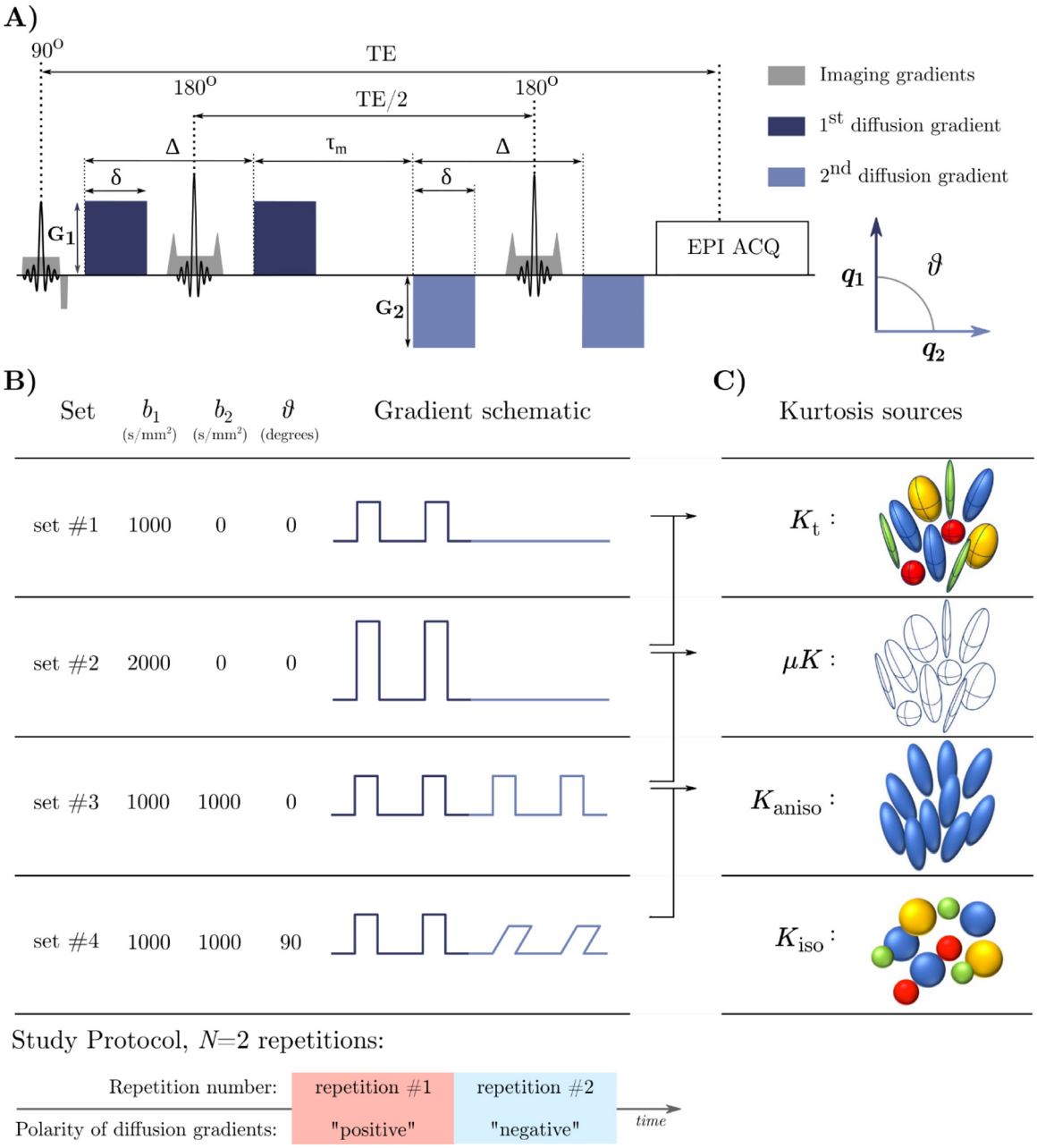

Fig. 1. CTI methodology. (A) DDE sequence adopted in this study. Abbreviations: TE: Echo Time; EPI ACQ: Echo Planar Imaging acquisition module. (B) CTI acquisition scheme. DDE set #1 and DDE set #2 mimic conventional SDE sequences. The additional DDE set #3 and DDE set #4 are respectively parallel and perpendicular DDE preparations, and they allow to disentangle the total Kurtosis (K_t) in its Kurtosis sources. (C) Kurtosis sources, adapted from Henriques et al., 2020. K_t can be decomposed into: (i) the microscopic kurtosis (μK), arising from non-Gaussianity induced by restricted time-dependent diffusion, structural disorder such as variations in compartmental cross-sectional area, or exchange effects, which can also be directly accessed through the combination of DDE set #2 and DDE set #3 (see Eq. (3)); (ii) the anisotropic Kurtosis (K_{aniso}), arising from the variance in the eigenvalues describing the microdomain diffusion tensors, *i.e.* the diffusion tensor shape variance, which can also be directly estimated through the combination of DDE set #3 and DDE set #4 (see Eq. (4)); and (iii) the isotropic Kurtosis (K_{iso}), arising from the variance of the microdomain diffusion tensors' mean diffusivity; factoring out exchange, $K_t = K_{aniso} + K_{iso} + \mu K$ (Henriques et al., 2020, 2021c). The acquisition was repeated twice in the same session without repositioning, with opposite polarities of all the diffusion gradients, allowing to assess and mitigate low order effects of cross-terms with imaging gradients (Neeman et al., 1991; Lawrenz and Finsterbusch, 2011, 2013; Ianuş et al., 2018).

ing (distributions of the SNR values across the different participants are shown in Fig. S1).

Anatomical images: T1w images resulting from the root mean squared combination of the four ME-MPRAGE echoes were parcellated with FreeSurfer's v. 7.1 *recon-all* pipeline. The following Regions Of Interest (ROIs) were considered among the areas included in the FreeSurfer's parcellation for the quantitative analysis of each kurtosis source: Cerebro-Spinal Fluid (CSF) in lateral ventricles, cerebral White Matter (WM), cerebellar WM (WM_{CBM}), Grey Matter (GM), cerebellar Grey Matter (GM_{CBM}), Amygdala (AMG), Caudate (Cd), Hippocampus (HPC), Globus Pallidus (GP), Putamen (PU), and Thalamus (TH). Linear registrations between individual skull-stripped T1w images and the first pre-processed non-smoothed $b = 0$ volume were then computed in ANTs (Avants et al., 2008, 2011) and registration matrices were applied to the above listed ROIs in order to get them aligned with the CTI maps.

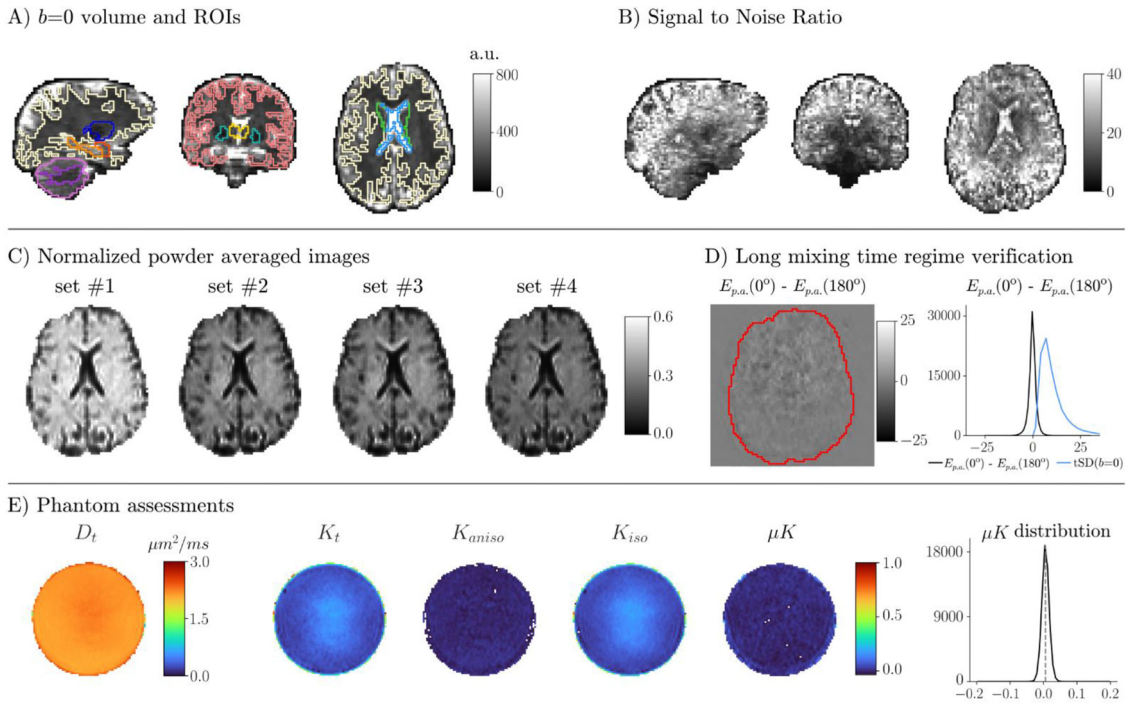

Fig. 2. Data quality. All brain images are from the same slices of a representative subject. (A) $b = 0$ volumes with overlaid borders of Regions of Interest (ROIs) used in this study. Lateral view: yellow: white matter; blue: putamen; orange: hippocampus; red: amygdala; light violet: cerebellar cortex; violet: cerebellar white matter. Coronal view: pink: cerebral cortex; yellow: thalamus; green: pallidum. Axial view: yellow: white matter; green: caudate; light blue: lateral ventricles. (B) Lateral, coronal, and axial view of the Signal to Noise Ratio map computed on $b = 0$ volumes ($SNR_{b=0}$) interspersed throughout all the DDE sets for a representative subject (the reader is referred to Section 2.4 *Image processing* for a description of the $SNR_{b=0}$ calculation). (C) Powder (*i.e.* directionally) averaged images per each set normalized by the mean $b = 0$ volumes ($p.a._{norm}$). (D) Left: map of the difference between parallel and antiparallel p.a. images at $b_t = 2000$ s/mm^2 with the brain border marked in red for a representative subject. Right: distribution of signal differences between the parallel and antiparallel p.a. images (black), with the distribution of the temporal standard deviation values across $b = 0$ shown in light blue, from the same subject. (E) CTI maps derived from the phantom experiment, and distribution of μK values within the phantom. Human data underwent the preprocessing pipeline described in the Materials and Methods section, and are shown before the application of the Gaussian smoothing (For interpretation of the references to color in this figure legend, the reader is referred to the web version of this article.).

Registration to MNI space and MNI-space CTI analysis: To obtain the first, high SNR group average templates of K_{aniso}, K_{iso}, and μK in the healthy human brain, CTI was fitted on across-subject averaged $p.a._{norm}$ signals warped to the MNI space. This approach was preferred rather than computing the average of individual CTI maps to avoid the propagation of noise in the individual maps to the final template.

To normalize each participant's $p.a._{norm}$ images to the MNI space, a symmetric diffeomorphic (non-linear) registration between each participant's skull-stripped T1w image and the MNI 2 mm-isotropic T1w brain atlas was computed. Finally, the resulting warp fields were applied to each $p.a._{norm}$ image in combination with the linear registration matrices previously computed to align the diffusion with the anatomical data (see *Anatomical images* Section), to get all the $p.a._{norm}$ images warped to the MNI space. All registration processes were carried out in ANTs (Avants et al., 2008, 2011) and were visually inspected for their accuracy. No Gaussian smoothing was applied on data that were normalized to the MNI space. Once all participants' $p.a._{norm}$ images were warped to the MNI space, the mean $p.a._{norm}$ image across $N = 8$ participants for each of the four DDE sets was computed and used for the CTI fit (hereafter referred to as *MNI-space CTI analysis*). Two subjects were excluded for the group MNI space analysis: i) one because of enlarged ventricles, and ii) because of unsuccessful alignment at the registration process.

Registrations' warp fields and matrices were also applied to the above listed FreeSurfer-derived ROIs (see *Anatomical images* Section), to warp them to MNI space. For each ROI, the intersection voxels across all $N = 8$ included participants were defined as ROIs for the MNI-space CTI analysis (hereafter referred to as $ROIs_{MNI}$), except for GM where voxels were included if common to at least six participants to get a more inclusive mask. Values derived from the MNI-space CTI analysis were then extracted from each ROI_{MNI} for the quantitative analysis of the Kurtosis sources and outlier values were removed with the isoutlier function (method: Grubbs) in MatLab version R2017b (The Mathworks Inc., Natwick, MA, USA). Finally, to assess the extent of each Kurtosis source contribution to K_t maps, the ratio between each Kurtosis source and K_t was computed, and values were extracted from each ROI for further analysis. Voxels with $K \leq 0$ (any kurtosis source) were excluded from this analysis (the ratio of excluded voxels on total voxels can be found in Fig. S2).

2.5. Correlation tensor imaging fit

The CTI fit procedure (described in Henriques et al., 2021c) was performed using the linear least square fit function in MatLab version R2017b. The CTI fit generates the following maps: D_t, K_t, K_{aniso}, K_{iso}, and μK maps. For each of these maps, values were extracted from each FreeSurfer-derived ROI (see *Anatomical images* Section) aligned to the diffusion space. Outlier values were removed with the isoutlier function (method: Grubbs) in MatLab R2017b, and mean and standard deviation (SD) values were computed per each ROI. For the phantom, values within an eroded phantom mask excluding voxels closer than 18 mm to the phantom surface were extracted.

2.6. MNI-space multiple Gaussian component (MGC) assumption analysis

To assess the effect of neglecting μK on the other Kurtosis sources and thus to explore the validity of the MGC assumption, similarly to

Table 1
CTI maps values for individual human and phantom data. Values correspond to mean ± one SD. For human data, the SD was computed across mean values of each participant's data. For phantom data, the SD was computed spatially, *i.e.* across all included phantom voxels. Abbreviations: CSF: Cerebrospinal fluid in lateral ventricles; WM: White Matter; WM_{CBM}: Cerebellar White Matter; GM: Grey Matter; GM_{CBM}: Cerebellar Grey Matter; AMG: Amygdala; Cd: Caudate; HPC: Hippocampus; GP: Globus Pallidus; PU: Putamen; TH: Thalamus.

Map	**Human data** Regions of Interest (ROIs)											**Phantom**
	CSF	WM	WM_{CBM}	GM	GM_{CBM}	AMG	Cd	HPC	GP	PU	TH	
D_t	3.47 ± 0.24	0.94 ± 0.02	0.87 ± 0.03	1.37 ± 0.11	1.20 ± 0.05	1.15 ± 0.05	1.48 ± 0.21	1.37 ± 0.07	0.86 ± 0.04	0.86 ± 0.02	1.21 ± 0.07	2.16 ± 0.11
K_t	0.49 ± 0.04	1.04 ± 0.02	1.23 ± 0.06	0.78 ± 0.01	0.97 ± 0.04	0.82 ± 0.04	0.83 ± 0.06	0.86 ± 0.03	1.54 ± 0.08	1.08 ± 0.05	1.1 ± 0.07	0.09 ± 0.04
K_{aniso}	0.02 ± 0.01	0.40 ± 0.03	0.48 ± 0.03	0.08 ± 0.01	0.10 ± 0.02	0.07 ± 0.01	0.06 ± 0.02	0.06 ± 0.01	0.26 ± 0.08	0.15 ± 0.03	0.21 ± 0.02	0.00 ± 0.01
K_{iso}	0.46 ± 0.03	0.47 ± 0.04	0.60 ± 0.07	0.57 ± 0.02	0.70 ± 0.05	0.60 ± 0.04	0.65 ± 0.05	0.69 ± 0.02	1.13 ± 0.13	0.73 ± 0.08	0.80 ± 0.08	0.08 ± 0.04
μK	0.01 ± 0.01	0.16 ± 0.01	0.15 ± 0.03	0.13 ± 0.02	0.18 ± 0.02	0.16 ± 0.01	0.12 ± 0.02	0.10 ± 0.01	0.15 ± 0.04	0.20 ± 0.02	0.10 ± 0.02	0.01 ± 0.01

Henriques et al. (2021c), K_{aniso} and K_{iso} were derived under the MGC assumption according to the tensor-valued information of the diffusion MRI acquisitions (Westin et al., 2014; Szczepankiewicz et al., 2019a). $p.a._{norm}$ images used for the *MNI-space CTI analysis* (thus only using axial tensor-valued experiments), were fitted with Eq. (5):

$$log\left(\bar{E}_{MGC}\left(b, b_\Delta\right)\right) = -b_t\bar{D} + \frac{1}{6}b_t^2\bar{D}^2K_{iso}^{MGC} + \frac{1}{6}b_t^2b_\Delta^2\bar{D}^2K_{aniso}^{MGC} + O\left(b^3\right) \quad (5)$$

with b_t representing the cumulative b-value (*i.e.* considering both pairs of diffusion gradients), and b_Δ being 1 for DDE sets #1-3 and −1/2 for DDE set #4.

2.7. MNI-space single-polarity CTI analysis

To assess effects of imaging cross-terms, $p.a._{norm}$ was computed separately on data corresponding to each polarity of the diffusion gradients (*i.e.* "positive" and "negative", Fig. 1B, bottom). $p.a._{norm}$ images then underwent the same registration pipeline described in the *Registration to MNI space and MNI-space CTI analysis* paragraph. μK values were extracted from each ROI for their quantitative analysis.

3. . Results

3.1. Data quality

Fig. 2A shows an example $b = 0$ volume with overlaid FreeSurfer-derived ROIs aligned to the diffusion space for a representative subject. Across subjects, mean $SNR_{b=0}$ ± one SD within the brain was 20 ± 1.35. Mean and SD values across subjects for $SNR_{b=0}$ and SNR_{PA} (for each set) for all ROIs can be found in Table S1, with their respective distribution shown in Fig. S1. The $SNR_{b=0}$ map and $p.a._{norm}$ images of non-smoothed data for a representative subject are shown in Fig. 2B and C, respectively. The difference between parallel and antiparallel gradient pairs designed to test for the long mixing time regime, is shown for a representative subject in Fig. 2D: the signal differences did not reveal visible anatomical structures for all sampled directions and were on the order of the tSD estimated on $b = 0$ volume in the same series.

3.2. Phantom study

CTI maps from the phantom (designed to ensure no systematic effects are observed) are shown in Fig. 2E (before Gaussian smoothing). Mean ± one SD values per each CTI map were: D_t: 2.16 ± 0.11; K_t: 0.09 ± 0.04; K_{aniso}: 0.00 ± 0.01; K_{iso}: 0.08 ± 0.04; μK: 0.01 ± 0.01; (see also Table 1).

3.3. Individual CTI maps analysis

Complete data from all participants were successfully acquired. Individual CTI-derived maps are shown in Fig. 3. Between subjects, maps consistently showed larger K_{aniso} values for white matter areas, larger K_{iso} values at the interface between tissues, and μK values that were centred on zero for CSF and non-vanishing positive for both grey and white matter. Across-subject mean ± one SD Diffusivity and Kurtosis values of CTI-derived maps are listed per each ROI in Table 1. Distributions of Diffusivity and Kurtosis values on individual maps per each ROI can be found on Fig. S3. Assessments of the relationship between all Kurtosis estimates and both SNR calculations considered ($SNR_{b=0}$ and SNR_{PA}) did not highlight dependencies of D_t, K_t, K_{aniso} and μK values on SNR, while a significant correlation was observed between K_{iso} and SNR (Fig. S4). Individual CTI-derived maps computed prior to the application of the smoothing are shown in Fig. S5.

3.4. MNI-space CTI analysis

CTI maps computed on across-subjects averaged $p.a._{norm}$ images are shown in Fig. 4A, along with distributions of values in each ROI (Fig. 4B). Consistently with individual-level maps, K_{aniso} was larger in WM regions, and K_{iso} was larger in regions that likely present higher degree of partial volume with CSF (regions near ventricles and edge of cortex); μK showed zero-centred values in CSF, but non-vanishing positive values both in grey and white matter (Table 2, voxels identified as outliers and excluded from the plotted distributions and quantitative analyses were < 3% for all ROIs and maps except for GP K_{aniso}, where excluded voxels represented 3.64% of total voxels; see Table S2 for number of excluded voxels and percentages on total voxels for all ROIs and maps). Fig. 5A–C shows maps of the ratio between each Kurtosis source and K_t, along with barplots showing the Kurtosis components per each ROI (Fig. 5D): K_{iso} appears to be the largest Kurtosis source for all tissues except white matter regions, with μK accounting for 8–20% of K_t in all ROIs except for CSF.

3.5. MNI-space CTI vs. MGC analysis

Fig. 6 shows the relationship between total, anisotropic and isotropic kurtosis estimates derived from CTI and the corresponding estimates under the MGC assumption, which neglects μK. For any of these metrics, a difference between the two approaches will be seen as a distribution that departs from the diagonal. Relative to CTI, the MGC approach leads to lower K_t in voxels with high μK. The opposite pattern was observed for K_{aniso} and K_{iso}, where estimates derived under the MGC assumption were overestimated compared to CTI-derived values, with larger deviations being associated to larger μK values.

3.6. MNI-space single-polarity CTI analysis

Fig. 7 shows CTI-derived maps from the averaged data corresponding to either both or single repetitions of the CTI acquisition. In comparison with maps estimated from two repetitions (corresponding to a ~52 min-long acquisition), maps computed from single repetitions suggest that there is no systematic bias when considering only one polarity of the diffusion gradients. Distributions of μK values derived from single repetitions per each ROI can be found in Fig. S6.

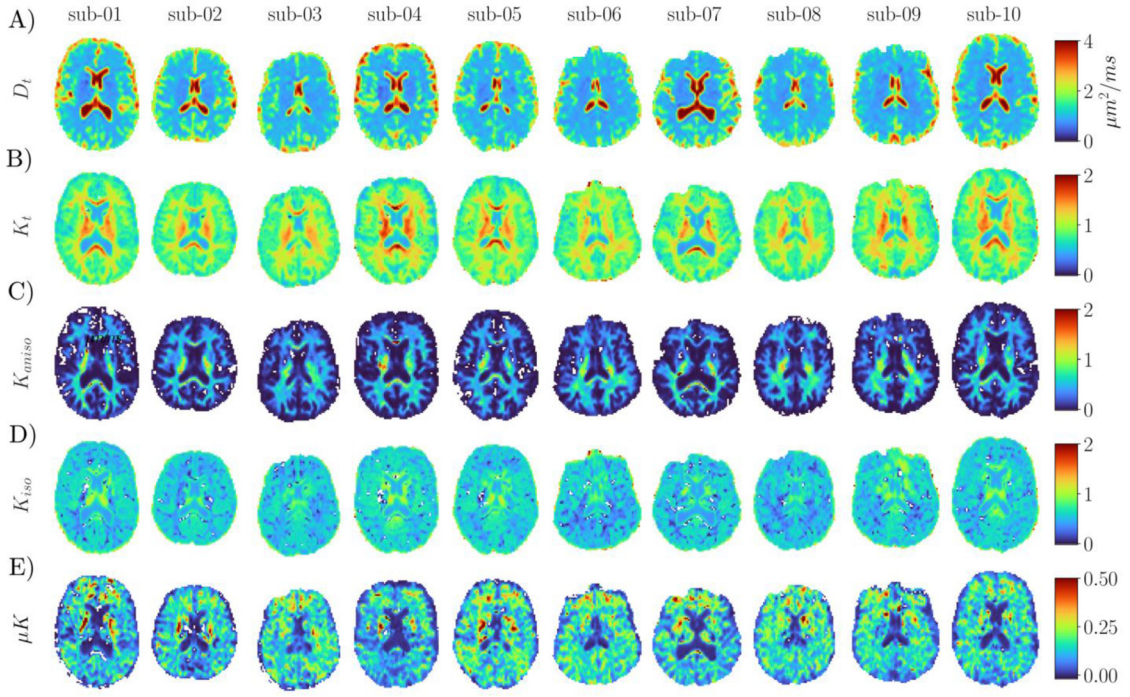

Fig. 3. Individual CTI-derived maps in native space. (A) D_t maps; (B) K_t maps; (C) K_{aniso} maps; (D) K_{iso} maps. White voxels within the brain correspond to negative K_{iso} values, possibly associated with noise effects; a discussion on negative kurtosis values can be found *e.g.* in Henriques et al. (2021d); (E) μK maps. Note the different ranges in the colorbars for different CTI metrics. All maps are shown in their native space, and no between-subject alignment was performed at this stage with the aim of displaying original values in the maps.

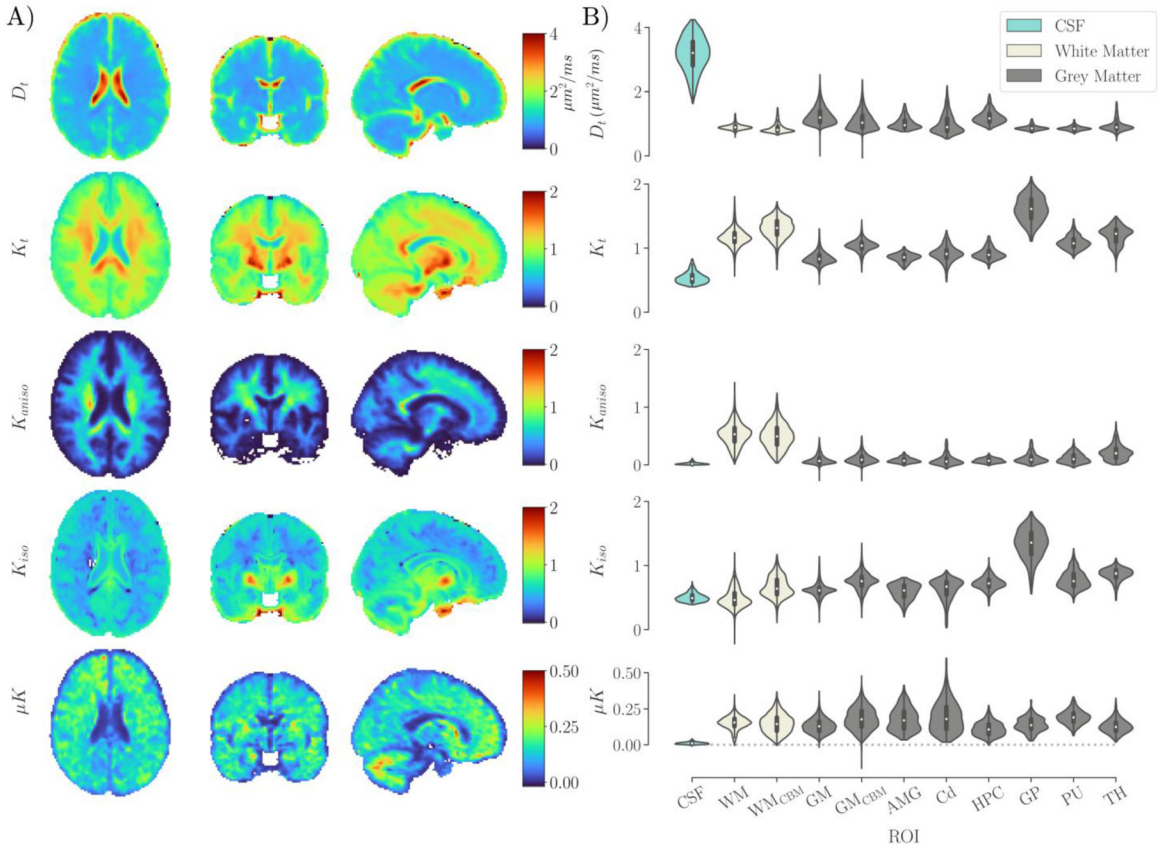

Fig. 4. CTI maps derived from the average of data from $N = 8$ subjects in MNI space (MNI-space CTI analysis). (A) Axial, coronal, and lateral (adjacent to mid-sagittal plane) views of D_t, K_t, K_{aniso}, K_{iso}, and μK maps derived by fitting the averaged data of $N = 8$ subjects, previously normalized to the 2 mm MNI atlas. Note the different ranges in the colorbars for different CTI metrics. (B) Distributions of values per each CTI metric in each Region of Interest (ROI) considered in this study. CSF: Cerebrospinal fluid in lateral ventricles; WM: White Matter; WM_{CBM}: Cerebellar White Matter; GM: Grey Matter; GM_{CBM}: Cerebellar Grey Matter; AMG: Amygdala; Cd: Caudate; HPC: Hippocampus; GP: Globus Pallidus; PU: Putamen; TH: Thalamus.

Table 2
Kurtosis sources values for CTI maps derived from the average of data from $N = 8$ subjects in MNI space (MNI-space CTI analysis). Values of K_t and of Kurtosis sources (K_{aniso}, K_{iso}, μK) correspond to mean ± one SD. Values of percent ratio between each Kurtosis source and K_t correspond to median (interquartile range, IQR). The SDs and the IQRs were computed spatially, *i.e.* across all included ROI voxels. Abbreviations: CSF: Cerebrospinal fluid in lateral ventricles; WM: White Matter; WM_{CBM}: Cerebellar White Matter; GM: Grey Matter; GM_{CBM}: Cerebellar Grey Matter; AMG: Amygdala; Cd: Caudate; HPC: Hippocampus; GP: Globus Pallidus; PU: Putamen; TH: Thalamus.

Map	Human group average template data: *MNI-space CTI analysis* Regions of Interest (ROIs)										
	CSF	WM	WM_{CBM}	GM	GM_{CBM}	AMG	Cd	HPC	GP	PU	TH
K_t	0.54 ± 0.09	1.17 ± 0.13	1.31 ± 0.15	0.84 ± 0.09	1.04 ± 0.09	0.85 ± 0.07	0.91 ± 0.12	0.91 ± 0.09	1.61 ± 0.19	1.09 ± 0.10	1.20 ± 0.14
K_{aniso}	0.02 ± 0.02	0.52 ± 0.19	0.50 ± 0.21	0.09 ± 0.08	0.10 ± 0.09	0.08 ± 0.04	0.08 ± 0.09	0.07 ± 0.04	0.12 ± 0.09	0.11 ± 0.08	0.21 ± 0.13
K_{aniso}/K_t % ratio	3.5 (3.9)	45.5 (17.2)	37.5 (18.6)	8.7 (9.6)	9.0 (8.7)	8.3 (6.9)	7.5 (9.9)	8.0 (5.8)	5.8 (6.5)	9.7 (11.6)	16.4 (11.3)
K_{iso}	0.50 ± 0.06	0.49 ± 0.15	0.67 ± 0.16	0.62 ± 0.11	0.75 ± 0.13	0.60 ± 0.12	0.63 ± 0.16	0.73 ± 0.10	1.34 ± 0.23	0.78 ± 0.14	0.86 ± 0.10
K_{iso}/K_t % ratio	94.5 (4.9)	40.4 (17.5)	48.7 (20.1)	75.3 (15.5)	73.8 (18.1)	70.3 (18.0)	70.8 (23.1)	80.2 (10.7)	85.7 (6.5)	71.7 (12.8)	73.0 (11.6)
μK	0.01 ± 0.01	0.15 ± 0.05	0.15 ± 0.07	0.13 ± 0.05	0.18 ± 0.08	0.18 ± 0.08	0.19 ± 0.10	0.11 ± 0.05	0.14 ± 0.05	0.19 ± 0.05	0.13 ± 0.05
$\mu K / K_t$ % ratio	1.9 (1.6)	13.2 (5.1)	10.8 (7.5)	15.0 (7.5)	17.0 (10.1)	19.6 (15.9)	17.9 (16.5)	11.6 (7.5)	8.2 (4.0)	17.3 (6.4)	10.1 (5.1)

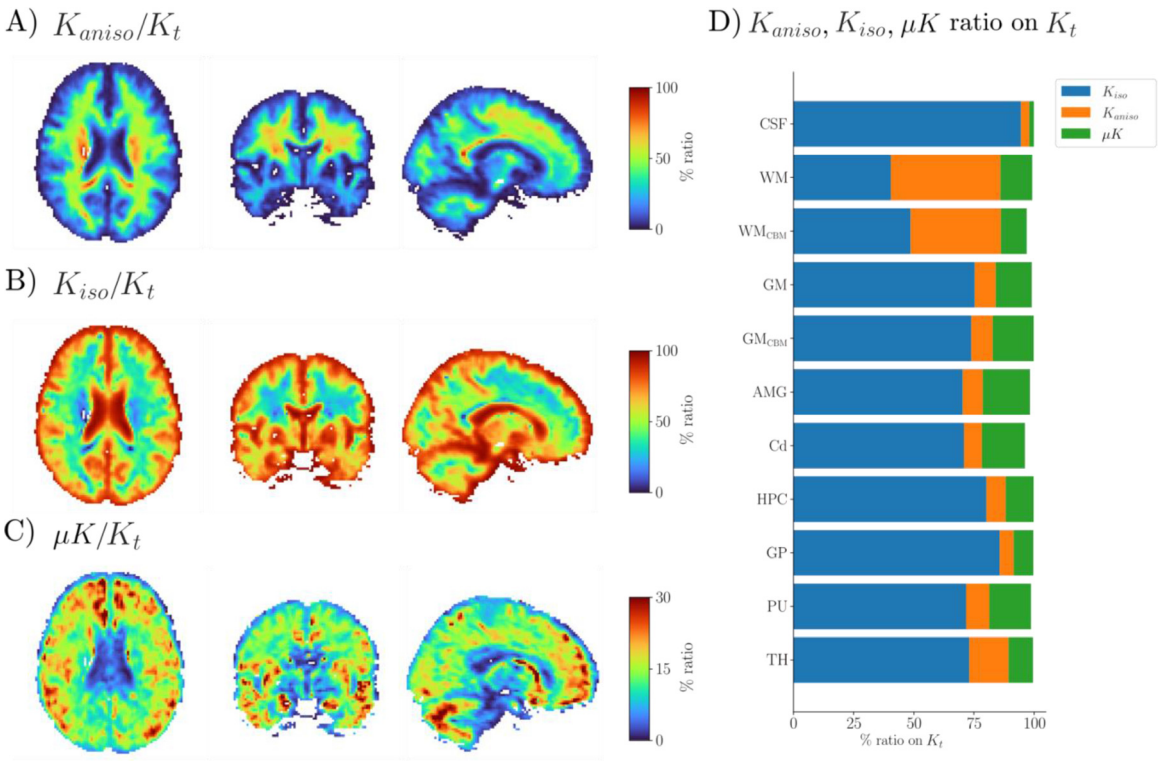

Fig. 5. Mapping the individual contribution of each source on total kurtosis. CTI maps derived from the average of data from $N = 8$ subjects in MNI space. Axial, coronal, and lateral (adjacent to mid-sagittal plane) views of (A) K_{aniso}/K_t ratio, (B) K_{iso}/K_t ratio, and (C) $\mu K/K_t$ ratio. Note the different ranges in the colorbars for different ratios. (D) Barplot showing median percent ratio per each Kurtosis source per each Region of Interest (ROI) considered in this study. CSF: Cerebrospinal fluid in lateral ventricles; WM: White Matter; WM_{CBM}: Cerebellar White Matter; GM: Grey Matter; GM_{CBM}: Cerebellar Grey Matter; AMG: Amygdala; Cd: Caudate; HPC: Hippocampus; GP: Globus Pallidus; PU: Putamen; TH: Thalamus.

4. . Discussion

Disentangling kurtosis sources in biological systems is attracting increasing interest given the potential to improve specificity and potentially provide novel non-invasive quantitative markers of microstructural properties *in vivo* (*e.g.* Szczepankiewicz et al., 2016; Yang et al., 2018; Nilsson et al., 2020; Kamiya et al., 2020). The recently-proposed CTI framework is designed to resolve anisotropic, isotropic, and microscopic kurtosis sources, which indeed provided much insight in preclinical imaging (Henriques et al., 2020, 2021c; Alves et al., 2022). In this work, we have extended the CTI methodology towards human imaging on a clinical 3T MRI system and aimed to investigate the kurtosis sources in healthy volunteers. Our main findings not only more accurately revealed the anisotropic and isotropic kurtosis sources in the human brain, but also clearly showed non-vanishing positive microscopic kurtosis contributions accounting for 8–20% of the total diffusional kurtosis in both white and grey matter, and vanishing in the ventricles (Figs. 3–5). Consistently with this finding, we also show differences in kurtosis estimates derived by neglecting microscopic kurtosis (Fig. 6). The results of the present study pave the way towards quantifying kurtosis sources more precisely and accurately, investigating them in different types of disease. Our findings motivate further developments to accelerate data acquisition to make human brain CTI more compatible with clinical scan times (*vide infra*).

4.1. Initial steps toward clinical translation

The first goal of this study was to evaluate the feasibility of using CTI in a clinical 3T system. Therefore, before performing CTI acquisitions in human volunteers, we tested our DDE sequence in water phantoms to confirm that the non-vanishing kurtosis sources do not arise from image artifacts or from noise Rician biases. The CTI experiments

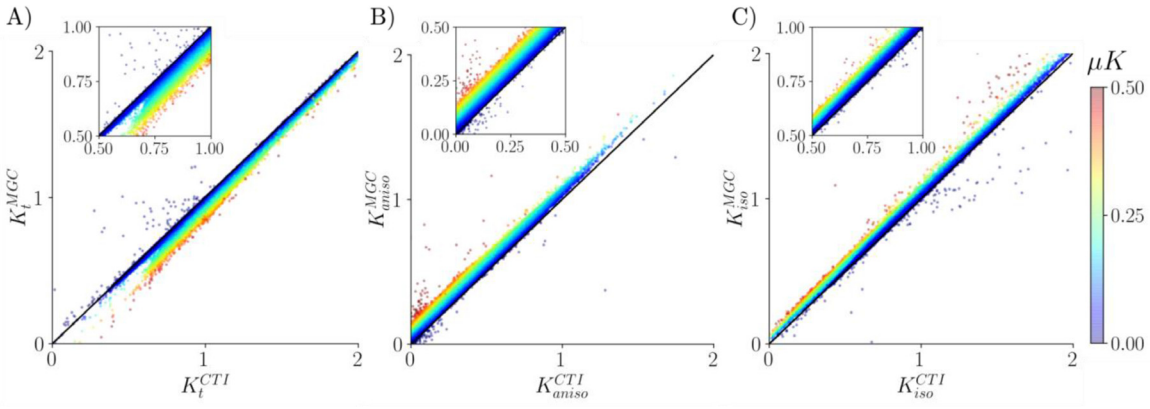

Fig. 6. Effect of neglecting μK on K_t, K_{aniso}, and K_{iso}. CTI- and MGC-derived maps were estimated on the average of data from $N = 8$ subjects in MNI space. (A) CTI- *vs.* MGC-derived K_t. (B) CTI- *vs.* MGC-derived K_{aniso}. (C) CTI- *vs.* MGC-derived K_{iso}. Points are colour-coded according to their μK value, inset plots are added for better visibility.

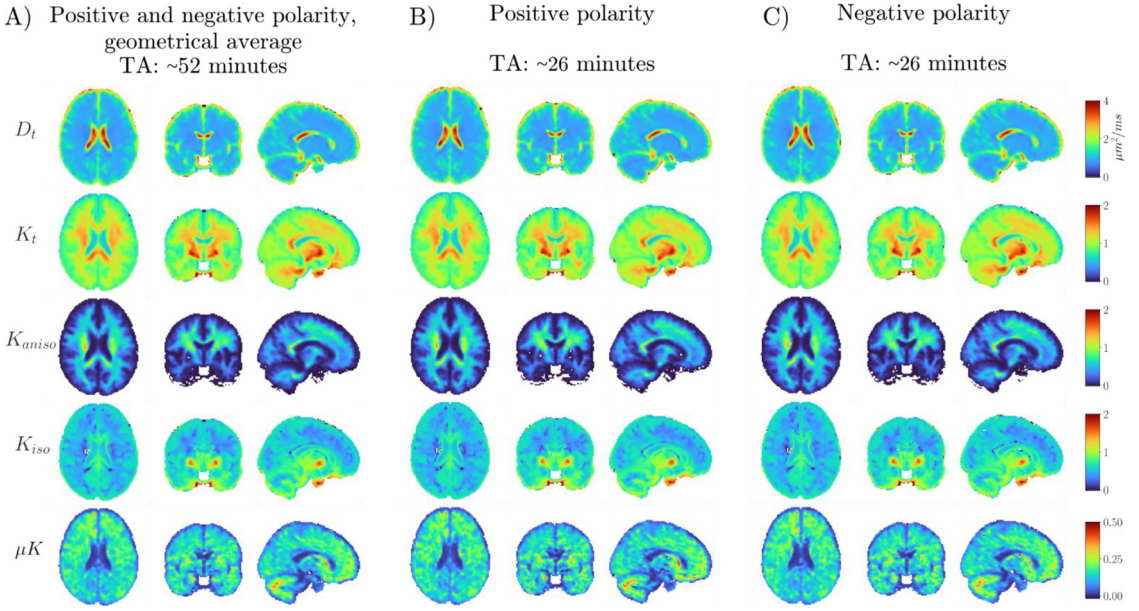

Fig. 7. Effect of reducing the acquisition time by 50% on CTI-derived maps. CTI-derived maps were estimated on the average of data from $N = 8$ subjects in MNI space. Axial, coronal, and lateral views of (A) CTI-derived maps estimated from the geometrical average of two repetitions, each acquired with opposite polarity of the diffusion gradients (here referred to as "positive" and "negative", Neeman et al., 1991; Ianuş et al., 2018), yielding a 52 min long acquisition; (B) CTI-derived maps estimated from only one repetition corresponding to the "positive" polarity of the diffusion gradients; (C) CTI-derived maps estimated from only one repetition corresponding to the "negative" polarity of the diffusion gradients. Note the different ranges in the colorbars for different CTI metrics. Acquisition time corresponding to only one repetition (panels B and C) was 26 min. TA: Acquisition time.

in the phantom corroborated the expected vanishing anisotropic kurtosis ($K_{aniso} = 0$) and vanishing microscopic kurtosis ($\mu K = 0$) of the free water phantom (Fig. 2E). It is important to note that, while it is anticipated that the water phantom exhibits free water diffusion with diffusivity around $2.13 \mu m^2/ms$ (assuming room temperature 22 °C; Mills 1973; Easteal et al., 1989) and zero non-Gaussian effects (all kurtosis sources are zero), such water phantom data is also expected to be corrupted by large Rician noise floor biases due to the fast signal decays of free water. From previous DKI studies (*e.g.* Jensen and Helpern, 2010; Glenn et al., 2015), it is known that Rician biases can lead to diffusion and kurtosis overestimations in these phantoms. These biases explain the small non-vanishing total kurtosis estimates observed in our water phantom data. Inspecting the different kurtosis sources, our results show that K_{iso} is the source that captures these biases, suggesting that K_{aniso} and μK are much less sensitive to these biases. Therefore, these results support that any non-vanishing K_{aniso} and μK observed in our *in vivo* human brain data has a microstructural origin. Analogously to the water phantom, these Rician biases also explain the overestimated diffusivities ($D_t > 3 \mu m^2/ms$) and non-vanishing K_t and K_{iso} observed in CSF regions of interest (Tables 1 and 2, Figs. 4B and 5B). While large Rician biases are expected for free water regions, this does not imply that D_t, K_t and K_{iso} are equally biased in brain tissues. Fig. S7 shows simulations representing the typical diffusivities/kurtosis values of free water, white matter and grey matter tissues. These simulations replicate the large biases in D_t, K_t and K_{iso} for the scenario representing free water at 22 °C (Fig. S7, A.1, A.2, A.4) and reveal much lower biases for typical values of white and grey matter (Fig. S7B,C) even for the lower SNR simulated (*i.e.* SNR = 10). Henriques et al., 2021c, further investigated the precision in μK estimation, and observed that for acquisition parameters in the same range as the ones adopted in the current study and SNR = 20, the expected error of μK for white and grey matter ranges between 0.1 and 0.2. While more advanced denoising techniques (*e.g.*

Eichner et al., 2015; Fadnavis et al., 2020) might alleviate this uncertainty range, both simulations in Henriques et al. (2021c) and the ones shown in Fig. S7, together with the absence of a correlation between SNR and μK (Fig. S4), suggest that, on the one hand, noise does affect the uncertainty range, but on the other hand, that it does not offset the μK distribution, thus lending further credibility to the observed positive μK values. Further research is needed to clarify the robustness of variations in μK – reconstructed from clinical scanners – possibly associated with different pathological processes. In preclinical settings in rat stroke models, Alves et al. (2022), reliably observed in stroke areas large increases in μK, larger in white matter, and corresponding decreases in D_t. While larger uncertainty in μK estimations is expected for systems with lower D_t and μK (Henriques et al., 2021c), whether similar patterns for increases in μK and decreases in D_t have counterbalancing or positive/negative effects on the robustness of the μK to noise in clinical systems remains to be investigated by future research.

In this first effort to translate CTI to a clinical scanner, we used the CTI acquisition scheme based on the minimal number of different gradient waveforms (c.f. Fig. 1B) proposed by Henriques et al. (2021c). However, for each different gradient waveform, we decided to use a relatively large number of gradient directions to ensure a high quality of powder averaged maps (c.f. Fig. 2C) and consequently a high-quality CTI reconstruction. This included 60 unique sets of SDE/DDE directions for each gradient waveform, which were repeated twice with opposite polarities to minimize cross-terms (using the geometrical average; Neeman et al., 1991; Lawrenz and Finsterbusch, 2011; Ianuş et al., 2018). This led to acquisition times of almost one hour per participant. We noticed, however, that our CTI reconstructions for the subset of the data containing only the "positive" polarity was qualitatively equal to the reconstruction from the subset of the data containing only the "negative" polarity (c.f. Fig. 7). This suggests that lower-order cross-terms imaging effects may be small in our data. Given this information, CTI acquisition can be accelerated by only acquiring data for a single polarity, which will reduce acquisition time by half. Further acceleration schemes reducing the number of parallel and perpendicular DDE directions are being developed and will be reported in due course.

In addition to the main acquisitions for CTI we also acquired data for 12 sets of antiparallel DDE experiments for a total b-value=2000 s/mm^2 to check the fulfillment of the long mixing time regime required for CTI (Henriques et al., 2020, 2021b). As discussed in previous literature (*e.g.* Özarslan, 2009; Jespersen, 2012), the long mixing time regime in theory is only completely met at infinitely long mixing times ($\tau_m \rightarrow \infty$); however, the CTI acquisitions in practice were performed for $\tau_m \approx \Delta \approx 32$ ms) for SNR optimization. Given this, checking the fulfillment of the long mixing time regime is crucial for this first translation of CTI to a clinical scanner (Shemesh and Cohen, 2011). This can be empirically done, by checking if data acquired with parallel and antiparallel DDE acquisitions is identical (*e.g.* Jespersen and Buhl, 2011; Koch and Finsterbusch, 2008; Özarslan, 2009; Ianuş et al., 2018; Henriques et al., 2020). Fig. 2D shows that the difference between parallel and perpendicular directions is negligible relative to the data Rician noise floor which suggests that the long mixing time regime is in practice met, *i.e.* no apparent time dependent effects as modelled by non-considered DDE correlation tensors Q and S are observed on our data (c.f. Jespersen, 2012; Henriques et al., 2020).

4.2. Value of separating kurtosis sources using the CTI methodology

The second objective of this study was to provide the first CTI kurtosis sources in human brain tissues. The obtained CTI maps showed consistent results across subjects (Fig. 3). Particularly, CTI total kurtosis K_t maps show the typical contrast observed by previous DKI studies (*e.g.* Jensen et al., 2005; Lu et al., 2006; Jensen and Helpern 2010; Veraart et al., 2013, Henriques et al., 2015, 2021a, 2021d) in which white matter regions show higher values than grey matter regions. Both results from individual maps (Fig. 3A) and group averaged templates (Fig. 4A) show that decomposing the total kurtosis into its underlying sources revealed specific complementary contrasts. For instance, while K_t maps show elevated values in regions where partial volume effects are expected, such as around the lateral ventricles, and in white matter regions where diffusion anisotropy is known to be high, the separation in sources allows to disentangle these different contributions – K_{iso} captures the high values due to high partial volume effects, while K_{aniso} shows the high values related to high microscopic anisotropy. Moreover, the CTI method enables the evaluation of μK (Jespersen et al., 2019; Henriques et al., 2020, 2021c; Alves et al., 2022) – a kurtosis source that is typically ignored by common microstructural models (*e.g.* Jespersen et al., 2007; Kaden et al., 2016; Novikov et al., 2018) and previous multi-dimensional encoding techniques based on the tensor-valued approach (*e.g.* Szczepankiewicz et al., 2015, Szczepankiewicz et al., 2019a, Topgaard, 2019). More specifically, with the diffusion times adopted in the current study, positive μK values were observed both for grey and white matter for both individual maps and the group average templates, suggesting that the kurtosis component arising from non-Gaussian effects might be ubiquitous in the cerebral tissue.

Although the main aim of the CTI analysis performed here was to provide a general inspection of the different kurtosis sources of human brains, in this study some regions of interest were arbitrary selected for a brief assessment of the kurtosis source regional differences (Figs. 2A and 4B). For instance, consistent with DKI studies, large K_t values were observed for the globus pallidus, which are likely a consequence of lower SNR due to the short T_2 characterizing this structure (Jensen and Helpern, 2010; Glenn et al., 2015). The source separation provided by CTI revealed that these large kurtosis values are due to K_{iso}- the metric that is expected to capture kurtosis noise biases (as explained above, c.f. Fig. S7). This motivates the use of advanced denoising techniques (*e.g.* Eichner et al., 2015; Fadnavis et al., 2020) and/or different fitting routines to decouple possible tissue-related effects from noise biases. Higher values of K_{aniso} were present in white matter, followed by the regions of the thalamus and of the globus pallidus, regions that are known to contain axonal fibers (Percheron et al., 1984; Byne et al., 2009); this result is consistent with the high shape variance expected in regions of white matter, and with previous descriptions of large microscopic anisotropy values in the human brain white matter (Lawrenz and Finsterbusch, 2015, 2019; Yang et al., 2018; Szczepankiewicz et al., 2019a). Regarding μK, all of our regions of interest showed values in the range between 0 and 0.3. It is important to note, however, that this apparent lack of μK variability may be a consequence of the coarse definition of regions of interest. Indeed, directly inspecting the maps in Fig. 4A, one can notice higher μK values in the cerebellar cortex which is known to contain well organized and densely-packed granule cells and bodies of large Purkinje cells – interestingly, this result is in line with lower signal decays observed on diffusion data acquired with high b-values and isotropic encodings (Tax et al., 2020). For a better qualitative inspection of the μK regional differences, additional slices of the averaged kurtosis source maps are presented in supplementary Fig. S8 with adjusted μK colormaps. This figure shows, for example, that μK values highlight the higher kurtosis values in the pre-frontal cortex reported on total kurtosis maps from early DKI studies (*e.g.* Jensen et al., 2005). On the other hand, low μK values can be qualitatively observed in the position of well-known white matter tracts such as the lateral projections of corpus callosum and the corticospinal tracts (note that these white matter regions are also associated to high K_{aniso} and low K_{iso}, suggesting that observed low μK values are unlikely explained by large CSF partial volume effects or low SNR). Although this observation may be useful to guide future explorations, the reproducibility of these exact regional differences and its biological interpretation is beyond the scope of this study. However, factors that may theoretically influence μK are presented below (see Section 4.4 "*μK as a new source of contrast*").

In summary, this study shows that disentangling diffusional kurtosis sources without *a priori* assumptions on the diffusion mode in the tissue represents an opportunity to enhance specificity in microstructural

imaging and to facilitate the detection of different biological processes that may not be visible in conventional DKI due to counterbalancing effects on its different sources. In future studies, we expect that separating diffusion kurtosis sources may be useful not only on resolving microstructural differences across distinct structures of healthy tissue but also on the characterization of the biological features of underlying pathophysiology, as already observed for predicting tumour histology (Szczepankiewicz et al., 2015, 2016; Nilsson et al., 2020) and for investigating the mechanisms of the early tissue responses to ischaemia (Alves et al., 2022). Moreover, from the perspective of the biophysical modelling of the dMRI signals, CTI could play a crucial role for the development of dMRI microstructural models: by providing an unbiased picture of signal features, this technique may help to set the ground for establishing adequate priors to be adopted in the modelling process and provide valid links between the detected signal features and their biological underpinnings (Novikov et al., 2018). Moreover, the increasingly available "orthogonal" diffusion-based contrasts provided by CTI's protocol may provide better fitting landscapes for microstructural modelling. Indeed, these aspect have been already explored by previous MDE preparations (*e.g.* De Santis et al., 2016; Lampinen et al., 2017; Jespersen et al., 2018; Henriques et al., 2019; Lampinen et al., 2019, 2021c, Alexander et al., 2017; Dyrby et al., 2018; Jespersen, 2018), and thus we expect that CTI provides an important framework to propel advances on all these fronts.

4.3. Comparison of CTI and MGC-driven approaches

The third objective of this study was to explore the implications of ignoring the μK component in our analysis. One common way to analyse multidimensional encoding data (MDE), including DDE acquisitions, is to assume that tissues can be represented by multiple Gaussian components, implicitly assuming $\mu K = 0$, and only use the b-tensor value encoded information provided by the diffusion preparation. Using the CTI methodology, our study provides clear evidence for residual non-Gaussian diffusion in the healthy adult human brain (the μK component, previously referred to as intra-compartmental kurtosis in Jespersen et al. (2019) and Henriques et al. (2020)) - particularly, our quantitative analysis suggests that μK accounts for between 8 and 20% of the total kurtosis (Fig. 5). Consistent with a previous pre-clinical CTI study (Henriques et al., 2021c), this study shows that if our DDE data is processed using only the MGC approximation and using only the b-tensor value encoding, μK propagates to other MDE-based estimates (Fig. 6).

As pointed out in a previous CTI study (Henriques et al., 2020), MDE approaches based on continuous q-trajectory waveforms may be advantageous on providing faster acquisitions than CTI. Therefore, information provided by CTI may be useful to understand how μK biases previous MDE framework and in which conditions these biases can be minimized. For instance, although in this study we only highlight how μK propagates on the MGC analysis if all data acquired for CTI is used, it was previously mathematically proved that μK biases can be suppressed on MGC K_{aniso} estimates if DDE acquisition with similar waveforms are used (Henriques et al., 2021c); however, with the expense of higher biases in MGC K_{iso} estimates (corresponding to the sum of two distinct kurtosis sources $K_{iso}^{MGC} = K_{iso}^{gt} + \mu K^{gt}/2$). Interestingly, our results revealed lower μK biases on MGC K_{aniso} and K_{iso} estimates than the biases observed by the previous pre-clinical study reported by Henriques et al. (2021c). These lower biases can be explained by the lower μK measured here, which is likely related to the different diffusion times probed in clinical systems (more information about the possible relationship between μK and diffusion time probed is discussed below in Section 4.4 "*μK as a new source of contrast*"). The lower μK biases observed in a clinical scanner is also in line with the lower time dependence biases observed by Szczepankiewicz et al. (2019b), relative to the pre-clinical time dependence biases observed by Jespersen et al. (2019). In future studies, CTI experiments can be used to measure μK biases on other acquisitions settings (including faster continuous q-trajectory waveforms) and on other tissue conditions (to note that μK biases can be more predominant in pathological tissues, such as in acute lesions (c.f. Alves et al., 2022)).

4.4. μK as a new source of contrast

Importantly, mapping the μK component, in addition to informing the frameworks neglecting non-Gaussian diffusion, represents a new source of contrast *per se*. By definition, indeed, the μK component represents the residual non-Gaussianity not captured by K_{aniso} and K_{iso}, which our current results suggest being ubiquitous in the human cerebral tissue, and, importantly, independent of the SNR spatial distribution. While the cellular underpinnings of the μK component remain to be elucidated by further research combined with histological assessments, several distinct phenomena might potentially underlie the positive μK values observed in our maps. For instance, simulations in Alves et al. (2022), demonstrate that neurite beading leads to positive μK values; these findings corroborate and clarify previous experimental observations in Budde and Frank (2010), and simulations in Skinner et al. (2015), who observed increases in kurtosis parallel to axons associated with beading in pathological axons. Variations in calibre are a physiological feature of axons (*e.g.* Dhital et al., 2018; Lee et al., 2019; Andersson et al., 2020), and future studies might investigate their potential contribution to the observed positive μK values. Nonetheless, other contributors might play a role in the observed positive μK values, such as bi-dimensional disorder in fibre packing (Burcaw et al., 2015), and potentially exchange (Fieremans et al., 2010; Nilsson et al., 2013; Ning et al., 2018; Olesen et al., 2022). The interplay of these potential contributors in yielding positive μK values, further enriched in complexity by the larger weights in ensemble μK of microdomains with larger diffusivity (c.f. $\mu K = \sum_i f_i \mu K_i D_i / D$ with f_i, μK_i and D_i being the individual apparent volume fraction, microscopic kurtosis and diffusivities of different microdomains, Henriques et al., 2020), gives rise to a rich yet intricate scenario. In white matter, increasing evidence points to larger parallel diffusivity in the intra-axonal domain as compared to the parallel diffusivity in the extra-axonal domain, but the intra- and extra-axonal domains, however, present with similar diffusion tensor traces due to their different radial components (Jelescu et al., 2020); nevertheless this picture is more complex in the grey matter, where exchange might be more prominent (*e.g.* Olesen et al., 2022), and in tissues presenting a mixture of grey matter and myelinated axons, such as several basal ganglia regions. This scenario, moreover, is further complicated by the potentially different relaxation times of different compartments, adding further relative weights f_i on the contributions of individual microdomains, and thus potentially significantly influencing the overall voxel-level μK. In this sense, future studies investigating possible associations of relaxation properties with microscopic diffusive dynamics or incorporating relaxation information in CTI might shed new light on the current findings, and potentially provide valuable information in clinical applications. In summary, in light of such a complex scenario, the observed relatively small variations in μK across histologically distinct brain regions might arise from different weights of μK contributors. Nevertheless, the ability to map the μK component in humans will prompt new investigations on the biological basis of μK, both in health and disease, where deviations from Gaussian diffusion could have a high value as biomarker (Lee et al., 2020b; Alves et al., 2022).

So far, in addition to studies directly investigating μK, insights on residual non-Gaussian diffusion mainly come from the works investigating diffusion and in turn kurtosis time-dependence. However, differently from the CTI approach, these require multiple measurements at different diffusion times, which can be onerous for clinical scanning. The observation of time-dependent diffusion, and in turn of kurtosis, indeed suggests that at least one tissue compartment exhibits non-Gaussian diffusion (Fieremans et al., 2016; Novikov et al., 2019; Lee et al., 2020a). Such deviations from Gaussianity are believed to be associated

with structural disorder and cross-sectional variance characterizing the sampled tissue (Novikov et al., 2014, see also below), and to be modulated by exchange effects (Ianuş et al., 2021; Nilsson et al., 2013; Ning et al., 2018; Olesen et al., 2022). It is important to point out that since the length scale of the displacements sensed by the diffusion encoding depends on the diffusion time (Δ) adopted (in addition to the substrate diffusion coefficient), at very long diffusion times the μK component might vanish due to the substrate's complete coarse-graining. In this situation, diffusion in each non-exchanging compartment then averages out and may be described as a Gaussian, and thus by a uniform effective diffusion coefficient (for a description of the diffusion phenomenon as a coarse-graining process see Novikov et al., 2019). Conversely, the μK component is expected to be increasingly important at short diffusion times, a regime at which more pronounced time-dependency has been observed (*e.g.* Fieremans et al., 2016; Jespersen et al., 2018). This short diffusion time regime is more easily achieved by high-performance gradients, such as those available in preclinical and dedicated human MRI systems (Aggarwal et al., 2012; Kunz et al., 2013; McNab et al., 2013b; Portnoy et al., 2013; Jones et al., 2018; Fan et al., 2020; Lee et al., 2020b; Henriques et al., 2021c; Huang et al., 2021); moreover, the μK component might be investigated at different length scales not only by varying the diffusion time of pulsed gradient pairs, but also alternatively by using oscillating waveforms at different frequencies, as done in DODE experiments (Ianuş et al., 2017, 2018; Shemesh, 2018), which might shed new light on the relative weight of μK at shorter time scales, and ultimately enrich our knowledge on its variations across multiple length scales.

Several pieces of evidence both from preclinical and clinical applications suggest the diagnostic potential of getting insights in such non-Gaussian diffusion components. For instance, in the preclinical setting, mapping the μK component in the rat brain post-ischaemia revealed enhanced sensitivity to stroke regions and allowed more specific insights into cellular mechanisms involved in response to stroke (Alves et al., 2022). In clinical systems, insights into such non-Gaussian diffusion in the human brain so far mainly come from studies investigating diffusion and kurtosis time-dependency. While several studies did not observe time-dependent diffusion effects in the *in vivo* human brain (Clark et al., 2001; Nilsson et al., 2009), other studies reported diffusion time-dependency both for white matter (Horsfield et al., 1994; Baron and Beaulieu, 2014; Van et al., 2014; Fieremans et al., 2016; Lee et al., 2018, 2020b; Grussu et al., 2019; Arbabi et al., 2020) and grey matter (Baron and Beaulieu, 2014; Lee et al., 2020a). Transverse to axonal bundles, time-dependent diffusion has been observed to report on two-dimensional structural disorder, in turn associated to the extra-axonal space packing geometry (Burcaw et al., 2015; Fieremans et al., 2016; Lee et al., 2018) and to be influenced by variations in axonal calibre, also referred to as axonal beading or varicosities (Ginsburger et al., 2018). Along axonal fibers, a stronger diffusion time-dependency has been observed to follow the power-law proposed in Novikov et al. (2014) for short-range disorder (Fieremans et al., 2016; Jespersen et al., 2018; Arbabi et al., 2020; Lee et al., 2020b). A link between the observed time-dependent signal modulations and their biological underpinnings is motivated by simulations of diffusion in three-dimensional reconstructions of histology-derived axonal segments, which clarified that the observed power-law time-dependency along axons arises in association with axonal varicosities (Lee et al., 2020b). Observations for a one-dimensional structural disorder power-law time dependency in grey matter, furthermore, suggest that this might be a universal property of the neural tissue (Does et al., 2003; Novikov et al., 2014; Lee et al., 2020a, 2020b).

4.5. Limitations

As any study, our work also has several limitations. For our phantom validation, we adopted an isotropic homogeneous phantom characterized by Gaussian diffusion. While our results confirm the expected Gaussian-only diffusion both in the phantom and in the lateral ventricles in the brain, the development of realistic phantoms with different levels of disordered structures mimicking the salient microstructural features believed to be associated with the μK component would be beneficial and support the current findings. The development of phantoms is an active and crucial branch in the field of the study of microstructure with dMRI (*e.g.* Shemesh et al., 2010b; Shemesh et al., 2012a; Nilsson et al., 2017; Fieremans and Lee, 2018; Giménez et al., 2018). Several studies have used numerical phantoms to investigate dMRI signal modulations associated with non-Gaussianity arising from restrictions or structural disorder (Ginsburger et al., 2018; Palombo et al., 2018; Henriques et al., 2020; Lee et al., 2020b, 2020c; Henriques et al., 2021c; Alves et al., 2022). However, increasing evidence for the accessibility to these microscopic disorder features via dMRI should prompt new crucial advancements in the manufacturing of physical phantoms allowing a further validation of the multiple kurtosis sources.

In addition, when performing the demonstrative MNI-space single-polarity CTI analysis, data were preprocessed considering both polarities. Future studies should investigate further the impact of reducing the number of directions on the CTI metrics estimation by considering accordingly the subset of data in the whole preprocessing stream.

Furthermore, potential effects of cross-terms with imaging gradients have been mitigated by taking the geometrical average of images corresponding to opposite polarities of the diffusion gradients, which however mitigates only low order effects of cross-terms. Nevertheless, the initial observation for qualitatively similar CTI-derived estimates when comparing geometrically-averaged maps with maps corresponding to single polarities (Fig. 7), together with the observation for expected values in maps derived on our water phantom experiment, suggest that possible residual uncorrected higher-order effects of cross-terms are likely to not introduce evident biases in the estimated parameters.

Another limitation is that the current framework assumes negligible exchange between tissue microdomains. More specifically, it should be noted that the microscopic kurtosis is currently estimated as the subtraction of the kurtosis arising from isotropic and anisotropic variances from the total kurtosis, leaving thus the possibility of exchange as a potential contributor. In other words, when two components (even if Gaussian) are exchanging in the time-scale of the diffusion experiment (diffusion time, mixing time in the case of CTI), then the total kurtosis and the Z-tensor will exhibit different terms associated with the exchange rates (Ning et al., 2018). On subtraction, the difference between these terms can generate a finite exchange-driven microscopic kurtosis. Thus, in principle, the microscopic kurtosis contrast could reflect kurtosis arising from microstructural geometry properties (*e.g.* cross sectional variance), exchange, or a combination of both (Olesen et al., 2022). Future studies should thus be designed to further disentangle these two effects and investigate more deeply the biological underpinnings of μK in the human brain. Nevertheless, separating the kurtosis arising from microscopic sources and variance in tensor magnitude and anisotropy is expected to be highly useful even before all the specific underpinnings are fully resolved (c.f. the sensitivity of microscopic kurtosis contrast in stroke).

5. Conclusions

This work demonstrates the translation of the CTI methodology from the preclinical to the clinical MRI setting, prompted by the increasing evidence suggesting the relevance of non-Gaussian diffusion in the characterization of the human brain microstructure. While non-Gaussian effects have been typically investigated by varying diffusion times, making such acquisitions potentially long and impractical, the CTI methodology offers a more practical alternative which has the potential to be further optimized for clinical applications. Mapping the microscopic kurtosis in human brain tissue for the first time revealed that, while until now commonly neglected, this component is non-vanishing. Consistent with this, we show that ignoring microscopic kurtosis affects the estimation of the other kurtosis components. The possibility of mapping

microscopic kurtosis in humans opens an intriguing new window on microscopic tissue features of great clinical and neuroscientific interest.

Data and code availability statement

Data and code used for data analysis are available via request to the authors, with the need of a formal sharing agreement.

Declaration of Competing Interest

L. Novello: None; R.N. Henriques: None; A. Ianuş: None; T. Feiweier: Thorsten Feiweier is an employee of Siemens Healthcare GmbH, owns stocks of Siemens (Healthineers) AG and holds patents filed by Siemens. N. Shemesh: None; J. Jovicich: None.

Credit authorship contribution statement

Lisa Novello: Conceptualization, Methodology, Validation, Formal analysis, Investigation, Writing – original draft, Writing – review & editing, Visualization, Data curation. **Rafael Neto Henriques:** Conceptualization, Methodology, Software, Investigation, Visualization, Writing – original draft, Writing – review & editing. **Andrada Ianuş:** Conceptualization, Methodology, Investigation, Visualization, Writing – original draft, Writing – review & editing, Funding acquisition. **Thorsten Feiweier:** Methodology, Software, Writing – review & editing. **Noam Shemesh:** Conceptualization, Investigation, Writing – original draft, Writing – review & editing, Supervision, Project administration, Funding acquisition. **Jorge Jovicich:** Conceptualization, Investigation, Writing – original draft, Writing – review & editing, Supervision, Resources, Project administration, Funding acquisition.

Acknowledgments

The authors thank Stefano Tambalo for support with data acquisition. This research was supported by the Caritro Foundation, Italy, the European Research Council (ERC) under the European Union's Horizon 2020 research and innovation programme (Starting Grant, agreement No. 679058), "la Caixa" Foundation (ID 100010434) and European Union's Horizon 2020 research and innovation programme under the Marie Skłodowska-Curie grant agreement No 847648, fellowship code CF/BQ/PI20/11760029.

Supplementary materials

Supplementary material associated with this article can be found, in the online version, at doi:10.1016/j.neuroimage.2022.119137.

References

Aggarwal, M., Jones, M.V., Calabresi, P.A., Mori, S., Zhang, J., 2012. Probing mouse brain microstructure using oscillating gradient diffusion MRI. Magn. Reson. Med. 67, 98–109. doi:10.1002/mrm.22981.

Alexander, D.C., Dyrby, T.B., Nilsson, M., Zhang, H., 2017. Imaging brain microstructure with diffusion MRI: practicality and applications. NMR Biomed. 1–26. doi:10.1002/nbm.3841.

Alves, R., Henriques, R.N., Kerkelä, L., Chavarrías, C., Jespersen, S.N., Shemesh, N., 2022. Correlation tensor MRI deciphers underlying kurtosis sources in stroke. Neuroimage 247, 118833. doi:10.1016/j.neuroimage.2021.118833.

Andersson, J.L.R., Skare, S., Ashburner, J., 2003. How to correct susceptibility distortions in spin-echo echo-planar images: application to diffusion tensor imaging. Neuroimage 20, 870–888. doi:10.1016/S1053-8119(03)00336-7.

Andersson, J.L.R., Sotiropoulos, S.N., 2016. An integrated approach to correction for off-resonance effects and subject movement in diffusion MR imaging. Neuroimage 125, 1063–1078. doi:10.1016/j.neuroimage.2015.10.019.

Andersson, M., Kjer, H.M., Rafael-Patino, J., Pacureanu, A., Pakkenberg, B., Thiran, J.P., Ptito, M., Bech, M., Dahl, A.B., Dahl, V.A., Dyrby, T.B., 2020. Axon morphology is modulated by the local environment and impacts the noninvasive investigation of its structure–function relationship. Proc. Natl. Acad. Sci. U. S. A. 117, 33649–33659. doi:10.1073/PNAS.2012533117.

Anwander, A., Tittgemeyer, M., Von Cramon, D.Y., Friederici, A.D., Knösche, T.R., 2007. Connectivity-based parcellation of Broca's area. Cereb. Cortex 17, 816–825. doi:10.1093/cercor/bhk034.

Arab, A., Wojna-Pelczar, A., Khairnar, A., Szabó, N., Ruda-Kucerova, J., 2018. Principles of diffusion kurtosis imaging and its role in early diagnosis of neurodegenerative disorders. Brain Res. Bull. 139, 91–98. doi:10.1016/J.BRAINRESBULL.2018.01.015.

Arbabi, A., Kai, J., Khan, A.R., Baron, C.A., 2020. Diffusion dispersion imaging: mapping oscillating gradient spin-echo frequency dependence in the human brain. Magn. Reson. Med. 83, 2197–2208. doi:10.1002/mrm.28083.

Assaf, Y., Cohen, Y., 1998. Non-mono-exponential attenuation of water and N-acetyl aspartate signals due to diffusion in brain tissue. J. Magn. Reson. 131, 69–85. doi:10.1006/jmre.1997.1313.

Assaf, Y., Pasternak, O., 2008. Diffusion tensor imaging (DTI)-based white matter mapping in brain research: a review. J. Mol. Neurosci. 34, 51–61. doi:10.1007/s12031-007-0029-0.

Avants, B.B., Epstein, C.L., Grossman, M., Gee, J.C., 2008. Symmetric diffeomorphic image registration with cross-correlation: evaluating automated labeling of elderly and neurodegenerative brain. Med. Image Anal. 12, 26–41. doi:10.1016/j.media.2007.06.004.

Avants, B.B., Tustison, N.J., Song, G., Cook, P.A., Klein, A., Gee, J.C., 2011. A reproducible evaluation of ANTs similarity metric performance in brain image registration. Neuroimage 54, 2033–2044. doi:10.1016/j.neuroimage.2010.09.025.

Baron, C.A., Beaulieu, C., 2014. Oscillating gradient spin-echo (OGSE) diffusion tensor imaging of the human brain. Magn. Reson. Med. 72, 726–736. doi:10.1002/mrm.24987.

Baron, C.A.lla., Kate, M., Gioia, L., Butcher, K., Emery, D., Budde, M., Beaulieu, C., 2015. Reduction of diffusion-weighted imaging contrast of acute ischemic stroke at short diffusion times. Stroke. 46, 2136–2141. doi:10.1161/STROKEAHA.115.008815.

Basser, P.J., Mattiello, J., LeBihan, D., 1994. MR diffusion tensor spectroscopy and imaging. Biophys. J. 66, 259–267. doi:10.1016/S0006-3495(94)80775-1.

Bastiani, M., Cottaar, M., Fitzgibbon, S.P., Suri, S., Alfaro-Almagro, F., Sotiropoulos, S.N., Jbabdi, S., Andersson, J.L.R., 2019. Automated quality control for within and between studies diffusion MRI data using a non-parametric framework for movement and distortion correction. Neuroimage 184, 801–812. doi:10.1016/j.neuroimage.2018.09.073.

Benetti, S., Novello, L., Maffei, C., Rabini, G., Jovicich, J., Collignon, O., 2018. White matter connectivity between occipital and temporal regions involved in face and voice processing in hearing and early deaf individuals. Neuroimage 179, 263–274. doi:10.1016/j.neuroimage.2018.06.044.

Blumenfeld-Katzir, T., Pasternak, O., Dagan, M., Assaf, Y., 2011. Diffusion MRI of structural brain plasticity induced by a learning and memory task. PLoS One 6. doi:10.1371/journal.pone.0020678.

Budde, M.D., Frank, J.A., 2010. Neurite beading is sufficient to decrease the apparent diffusion coefficient after ischemic stroke. Proc. Natl. Acad. Sci. U. S. A. 107, 14472–14477. doi:10.1073/pnas.1004841107.

Budde, M.D., Skinner, N.P., Tugan Muftuler, L., Schmit, B.D., Kurpad, S.N., 2017. Optimizing filter-probe diffusion weighting in the rat spinal cord for human translation. Front. Neurosci. 11, 1–13. doi:10.3389/fnins.2017.00706.

Burcaw, L.M., Fieremans, E., Novikov, D.S., 2015. Mesoscopic structure of neuronal tracts from time-dependent diffusion. Neuroimage 114, 18–37. doi:10.1016/j.neuroimage.2015.03.061.

Byne, W., Hazlett, E.A., Buchsbaum, M.S., Kemether, E., 2009. The thalamus and schizophrenia: current status of research. Acta Neuropathol. 117, 347–368. doi:10.1007/s00401-008-0404-0.

Callaghan, P., Coy, A., MacGowan, D., Packer, K.J., Zelaya, F.O., 1991. Diffraction-like effects in NMR diffusion studies of fluids in porous solids. Nature 351, 467–469. doi:10.1038/351467a0.

Callaghan, P.T., Komlosh, M.E., 2002. Locally anisotropic motion in a macroscopically isotropic system: displacement correlations measured using double pulsed gradient spin-echo NMR. Magn. Reson. Chem. 40, 15–19. doi:10.1002/mrc.1122.

Cheng, Y., Cory, D.G., 1999. Multiple scattering by NMR [3]. J. Am. Chem. Soc. 121, 7935–7936. doi:10.1021/ja9843324.

Clark, C.A., Hedehus, M., Moseley, M.E., 2001. Diffusion time dependence of the apparent diffusion tensor in healthy human brain and white matter disease. Magn. Reson. Med. 45, 1126–1129. doi:10.1002/mrm.1149.

Coelho, S., Pozo, J.M., Jespersen, S.N., Jones, D.K., Frangi, A.G., 2019. Resolving degeneracy in diffusion MRI biophysical model parameter estimation using double diffusion encoding. Magn. Reason. Med. 82 (1), 395–410. doi:10.1002/mrm.27714.

Cottaar, M., Szczepankiewicz, F., Bastiani, M., Hernandez-Fernandez, M., Sotiropoulos, S.N., Nilsson, M., Jbabdi, S., 2020. Improved fibre dispersion estimation using b-tensor encoding. Neuroimage 215, 116832. doi:10.1016/j.neuroimage.2020.116832.

De Santis, S., Jones, D.K., Roebroeck, A., 2016. Including diffusion time dependence in the extra-axonal space improves *in vivo* estimates of axonal diameter and density in human white matter. Neuroimage 130, 91–103. doi:10.1016/j.neuroimage.2016.01.047.

Delgado, A.F., Nilsson, M., Van Westen, D., Delgado, A.F., 2018. Glioma grade discrimination with MR diffusion kurtosis imaging: a meta-Analysis of diagnostic accuracy. Radiology 287, 119–127. doi:10.1148/radiol.2017171315.

Della-Maggiore, V., Scholz, J., Johansen-Berg, H., Paus, T., 2009. The rate of visuomotor adaptation correlates with cerebellar white-matter microstructure. Hum. Brain Mapp. 30, 4048–4053. doi:10.1002/hbm.20828.

Dhital, B., Kellner, E., Kiselev, V.G., Reisert, M., 2018. The absence of restricted water pool in brain white matter. Neuroimage 182, 398–406. doi:10.1016/j.neuroimage.2017.10.051.

Does, M.D., Parsons, E.C., Gore, J.C., 2003. Oscillating gradient measurements of water diffusion in normal and globally ischemic rat brain. Magn. Reson. Med. 49, 206–215. doi:10.1002/mrm.10385.

Dyrby, T.B., Innocenti, G., Bech, M., Lundell, H., 2018. Validation strategies for the interpretation of microstructure imaging using diffusion MRI. Neuroimage doi:10.1016/j.neuroimage.2018.06.049.

Eichner, C., Cauley, S.F., Cohen-Adad, J., Möller, H.E., Turner, R., Setsompop, K., Wald, L.L., 2015. Real diffusion-weighted MRI enabling true signal averaging and increased diffusion contrast. Neuroimage 122, 373–384. doi:10.1016/j.neuroimage.2015.07.074.

Easteal, A.J., Price, W.E., Woolf, L.A., 1989. Diaphragm cell for high-temperature diffusion measurements. J. Chem. Soc. Faraday Trans. 1 85 (5), 1091–1097. doi:10.1039/F19898501091.

Eriksson, S., Lasic, S., Topgaard, D., 2013. Isotropic diffusion weighting in PGSE NMR by magic-angle spinning of the q-vector. J. Magn. Reson. 226, 13–18. doi:10.1016/J.JMR.2012.10.015.

Fadnavis, S., Batson, J., Garyfallidis, E., 2020. Patch2Self: denoising diffusion MRI with self-supervised learning. Adv. Neural Inf. Process. Syst. 33, 16293–16303.

Falangola, M.F., Jensen, J.H., Babb, J.S., Hu, C., Castellanos, F.X., Di Martino, A., Ferris, S.H., Helpern, J.A., 2008. Age-related non-Gaussian diffusion patterns in the prefrontal brain. J. Magn. Reson. Imaging 28, 1345–1350. doi:10.1002/jmri.21604.

Fan, Q., Witzel, T., Tounekti, S., Tian, Q., Ngamsombat, C., Polackal, M., Nummenmaa, A., Huang, S.Y., 2020. Investigating restricted diffusion within different cortical regions using double-diffusion encoding. In: Proceedings of the International Society for Magnetic Resonance in Medicine.

Fieremans, E., Benitez, A., Jensen, J.H., Falangola, M.F., Tabesh, A., Deardorff, R.L., Spampinato, M.V.S., Babb, J.S., Novikov, D.S., Ferris, S.H., Helpern, J.A., 2013. Novel white matter tract integrity metrics sensitive to Alzheimer disease progression. Am. J. Neuroradiol. 34, 2105–2112. doi:10.3174/ajnr.A3553.

Fieremans, E., Burcaw, L.M., Lee, H.H., Lemberskiy, G., Veraart, J., Novikov, D.S., 2016. *In vivo* observation and biophysical interpretation of time-dependent diffusion in human white matter. Neuroimage 129, 414–427. doi:10.1016/j.neuroimage.2016.01.018.

Fieremans, E., Jensen, J.H., Helpern, J.A., 2011. White matter characterization with diffusional kurtosis imaging. Neuroimage 58, 177–188. doi:10.1016/j.neuroimage.2011.06.006.

Fieremans, E., Lee, H.H., 2018. Physical and numerical phantoms for the validation of brain microstructural MRI: a cookbook. Neuroimage doi:10.1016/j.neuroimage.2018.06.046.

Fieremans, E., Novikov, D.S., Jensen, J.H., Helpern, J.A., 2010. Monte Carlo study of a two-compartment exchange model of diffusion. NMR Biomed. 23 (7), 711–724. doi:10.1002/nbm.1577.

Gauvain, K.M., McKinstry, R.C., Mukherjee, P., Perry, A., Neil, J.J., Kaufman, B.A., Hayashi, R.J., 2001. Evaluating pediatric brain tumor cellularity with diffusion-tensor imaging. Am. J. Roentgenol. 177, 449–454. doi:10.2214/ajr.177.2.1770449.

Glenn, G.R., Tabesh, A., Jensen, J.H., 2015. A simple noise correction scheme for diffusional kurtosis imaging. Magn. Reson. Imaging 33 (1), 124–133. doi:10.1016/j.mri.2014.08.028.

Giménez, M.L., Jiménez, P., Pedraza Pérez, L.A., Betancourth, D., Zwick, A., Álvarez, G.A., 2018. Microstructure size-distribution estimations with smooth and sharp non-uniform oscillating gradient spin-echo modulations. In: Proceedings of the International Society for Magnetic Resonance in Medicine.

Ginsburger, K., Poupon, F., Beaujoin, J., Estournet, D., Matuschke, F., Mangin, J.F., Axer, M., Poupon, C., 2018. Improving the realism of white matter numerical phantoms: a step toward a better understanding of the influence of structural disorders in diffusion MRI. Front. Phys. 5. doi:10.3389/fphy.2018.00012.

Gong, N.J., Wong, C.S., Chan, C.C., Leung, L.M., Chu, Y.C., 2013. Correlations between microstructural alterations and severity of cognitive deficiency in Alzheimer's disease and mild cognitive impairment: a diffusional kurtosis imaging study. Magn. Reson. Imaging 31, 688–694. doi:10.1016/J.MRI.2012.10.027.

Grussu, F., Ianuş, A., Tur, C., Prados, F., Schneider, T., Kaden, E., Ourselin, S., Drobnjak, I., Zhang, H., Alexander, D.C., Gandini Wheeler-Kingshott, C.A.M., 2019. Relevance of time-dependence for clinically viable diffusion imaging of the spinal cord. Magn. Reson. Med. 81, 1247–1264. doi:10.1002/mrm.27463.

Hardin, R.H., Sloane, N.J.A.A., 1996. McLaren's improved snub cube and other new spherical designs in three dimensions. Discret. Comput. Geom. 15, 429–441.

Hasan, K.M., Mwangi, B., Keser, Z., Riascos, R., Sargsyan, A.E., Kramer, L.A., 2018. Brain quantitative MRI metrics in astronauts as a unique professional group. J. Neuroimaging 28, 256–268. doi:10.1111/jon.12501.

Helpern, J.A., Adisetiyo, V., Falangola, M.F., Hu, C., Di Martino, A., Williams, K., Castellanos, F.X., Jensen, J.H., 2011. Preliminary evidence of altered gray and white matter microstructural development in the frontal lobe of adolescents with attention-deficit hyperactivity disorder: a diffusional kurtosis imaging study. J. Magn. Reson. Imaging 33, 17–23. doi:10.1002/jmri.22397.

Hempel, J.M., Bisdas, S., Schittenhelm, J., Brendle, C., Bender, B., Wassmann, H., Skardelly, M., Tabatabai, G., Vega, S.C., Ernemann, U., Klose, U., 2017. *In vivo* molecular profiling of human glioma using diffusion kurtosis imaging. J. Neurooncol. 131, 93–101. doi:10.1007/s11060-016-2272-0.

Hempel, J.M., Schittenhelm, J., Bisdas, S., Brendle, C., Bender, B., Bier, G., Skardelly, M., Tabatabai, G., Castaneda Vega, S., Ernemann, U., Klose, U., 2018. *In vivo* assessment of tumor heterogeneity in WHO 2016 glioma grades using diffusion kurtosis imaging: diagnostic performance and improvement of feasibility in routine clinical practice. J. Neuroradiol. 45, 32–40. doi:10.1016/J.NEURAD.2017.07.005.

Henriques, R.N., 2018. Advanced Methods for Diffusion MRI Data Analysis and Their Application to The Healthy Ageing Brain. University of Cambridge doi:10.17863/CAM.29356.

Henriques, R.N., Correia, M.M., Marrale, M., Huber, E., Kruper, J., Koudoro, S., Yeatman, J.D., Garyfallidis, E., Rokem, A., 2021a. Diffusional kurtosis imaging in the diffusion imaging in python project. Front. Hum. Neurosci. 15. doi:10.3389/fnhum.2021.675433.

Henriques, R.N., Correia, M.M., Nunes, R.G., Ferreira, H.A., 2015. Exploring the 3D geometry of the diffusion kurtosis tensor—impact on the development of robust tractography procedures and novel biomarkers. Neuroimage 111, 85–99. doi:10.1016/J.NEUROIMAGE.2015.02.004.

Henriques, R.N., Jespersen, S.N., Jones, D.K., Veraart, J., 2021d. Toward more robust and reproducible diffusion kurtosis imaging. Magn. Reson. Med. 86, 1600–1613. doi:10.1002/mrm.28730.

Henriques, R.N., Jespersen, S.N., Shemesh, N., 2020. Correlation tensor magnetic resonance imaging. Neuroimage 211. doi:10.1016/j.neuroimage.2020.116605.

Henriques, R.N., Jespersen, S.N., Shemesh, N., 2019. Microscopic anisotropy misestimation in spherical-mean single diffusion encoding MRI. Magn. Reson. Med. 81, 3245–3261. doi:10.1002/mrm.27606.

Henriques, R.N., Palombo, M., Jespersen, S.N., Shemesh, N., Lundell, H., Ianuş, A., 2021b. Double diffusion encoding and applications for biomedical imaging. J. Neurosci. Methods, 108989 doi:10.1016/j.jneumeth.2020.108989.

Henriques, R.N., Jespersen, S.N., Shemesh, N., 2021c. Evidence for microscopic kurtosis in neural tissue revealed by correlation tensor MRI. Magn. Reson. Med. 1–20. doi:10.1002/mrm.28938.

Horsfield, M.A., Barker, G.J., McDonald, W.I., 1994. Self-diffusion in CNS tissue by volume-selective proton NMR. Magn. Reson. Med. 31, 637–644. doi:10.1002/mrm.1910310609.

Huang, S.Y., Witzel, T., Keil, B., Scholz, A., Davids, M., Dietz, P., Rummert, E., Ramb, R., Kirsch, J.E., Yendiki, A., Fan, Q., Tian, Q., Ramos-Llordén, G., Lee, H.H., Nummenmaa, A., Bilgic, B., Setsompop, K., Wang, F., Avram, A.V., Komlosh, M., Benjamini, D., Magdoom, K.N., Pathak, S., Schneider, W., Novikov, D.S., Fieremans, E., Tounekti, S., Mekkaoui, C., Augustinack, J., Berger, D., Shapson-Coe, A., Lichtman, J., Basser, P.J., Wald, L.L., Rosen, B.R., 2021. Connectome 2.0: developing the next-generation ultra-high gradient strength human MRI scanner for bridging studies of the micro-, meso- and macro-connectome. Neuroimage 243, 118530. doi:10.1016/j.neuroimage.2021.118530.

Huber, E., Henriques, R.N., Owen, J.P., Rokem, A., Yeatman, J.D., 2019. Applying microstructural models to understand the role of white matter in cognitive development. Dev. Cogn. Neurosci. 36, 100624. doi:10.1016/J.DCN.2019.100624.

Hui, E.S., Fieremans, E., Jensen, J.H., Tabesh, A., Feng, W., Bonilha, L., Spampinato, M.V., Adams, R., Helpern, J.A., 2012. Stroke assessment with diffusional kurtosis imaging. Stroke 43, 2968–2973. doi:10.1161/STROKEAHA.112.657742.

Ianuş, A., Alexander, D.C., Zhang, H., Palombo, M., 2021. Mapping complex cell morphology in the grey matter with double diffusion encoding MR: a simulation study. Neuroimage 241, 118424. doi:10.1016/J.NEUROIMAGE.2021.118424.

Ianuş, A., Drobnjak, I., Alexander, D.C., 2016. Model-based estimation of microscopic anisotropy using diffusion MRI: a simulation study. NMR Biomed. 29, 672–685. doi:10.1002/nbm.3496.

Ianuş, A., Jespersen, S.N., Serradas Duarte, T., Alexander, D.C., Drobnjak, I., Shemesh, N., 2018. Accurate estimation of microscopic diffusion anisotropy and its time dependence in the mouse brain. Neuroimage 183, 934–949. doi:10.1016/j.neuroimage.2018.08.034.

Ianuş, A., Shemesh, N., Alexander, D.C., Drobnjak, I., 2017. Double oscillating diffusion encoding and sensitivity to microscopic anisotropy. Magn. Reson. Med. 78, 550–564. doi:10.1002/mrm.26393.

Jacobacci, F., Armony, J.L., Yeffal, A., Lerner, G., Amaro, E., Jovicich, J., Doyone, J., Della-Maggiore, V., 2020. Rapid hippocampal plasticity supports motor sequence learning. Proc. Natl. Acad. Sci. U. S. A. 117, 23898–23903. doi:10.1073/pnas.2009576117.

Jelescu, I.O., Veraart, J., Adisetiyo, V., Milla, S.S., Novikov, D.S., Fieremans, E., 2015. One diffusion acquisition and different white matter models: how does microstructure change in human early development based on WMTI and NODDI? Neuroimage 107, 242–256. doi:10.1016/J.NEUROIMAGE.2014.12.009.

Jelescu, I.O., Veraart, J., Fieremans, E., Novikov, D.S., 2016. Degeneracy in model parameter estimation for multi-compartmental diffusion in neuronal tissue. NMR Biomed. 29, 33–47. doi:10.1002/nbm.3450.

Jelescu, I.O., Palombo, M., Bagnato, F., Schilling, K.G., 2020. Challenges for biophysical modeling of microstructure. J. Neurosci. Methods 344, 108861. doi:10.1016/j.jneumeth.2020.108861.

Jensen, J.H., Helpern, J.A., 2010. MRI quantification of non-Gaussian water diffusion by kurtosis analysis. NMR Biomed. doi:10.1002/nbm.1518.

Jensen, J.H., Helpern, J.A., Ramani, A., Lu, H., Kaczynski, K., 2005. Diffusional kurtosis imaging: the quantification of non-Gaussian water diffusion by means of magnetic resonance imaging. Magn. Reson. Med. 53, 1432–1440. doi:10.1002/mrm.20508.

Jespersen, S.N., Kroenke, C.D., Østergaard, L., Ackerman, J.J.H., Yablonskiy, D.A., 2007. Modeling dendrite density from magnetic resonance diffusion measurements. Neuroimage 34, 1473–1486. doi:10.1016/j.neuroimage.2006.10.037.

Jespersen, S.N., 2018. White matter biomarkers from diffusion MRI. J. Magn. Reson. 291, 127–140. doi:10.1016/J.JMR.2018.03.001.

Jespersen, S.N., 2012. Equivalence of double and single wave vector diffusion contrast at low diffusion weighting. NMR Biomed. 25, 813–818. doi:10.1002/nbm.1808.

Jespersen, S.N., Buhl, N., 2011. The displacement correlation tensor: microstructure, ensemble anisotropy and curving fibers. J. Magn. Reson. 208, 34–43. doi:10.1016/j.jmr.2010.10.003.

Jespersen, S.N., Lundell, H., Sønderby, C.K., Dyrby, T.B., 2013. Orientationally invariant metrics of apparent compartment eccentricity from double pulsed field gradient diffusion experiments. NMR Biomed. 26, 1647–1662. doi:10.1002/nbm.2999.

Jespersen, S.N., Olesen, J.L., Hansen, B., Shemesh, N., 2018. Diffusion time dependence of microstructural parameters in fixed spinal cord. Neuroimage 182, 329–342. doi:10.1016/j.neuroimage.2017.08.039.

Jespersen, S.N., Olesen, J.L., Ianuş, A., Shemesh, N., 2019. Effects of nongaussian diffusion on "isotropic diffusion" measurements: an *ex-vivo* microimaging and simulation study. J. Magn. Reson. 300, 84–94. doi:10.1016/J.JMR.2019.01.007.

Johansen-Berg, H., 2010. Behavioural relevance of variation in white matter microstructure. Curr. Opin. Neurol. 23, 351–358. doi:10.1097/WCO.0b013e32833b7631.

Jones, D.K., Alexander, D.C., Bowtell, R., Cercignani, M., Dell'Acqua, F., McHugh, D.J., Miller, K.L., Palombo, M., Parker, G.J.M., Rudrapatna, U.S., Tax, C.M.W., 2018. Microstructural imaging of the human brain with a 'super-scanner': 10 key advantages of ultra-strong gradients for diffusion MRI. Neuroimage 182, 8–38. doi:10.1016/j.neuroimage.2018.05.047.

Kaden, E., Kelm, N.D., Carson, R.P., Does, M.D., Alexander, D.C., 2016. Multi-compartment microscopic diffusion imaging. Neuroimage 139, 346–359. doi:10.1016/j.neuroimage.2016.06.002.

Kamagata, K., Tomiyama, H., Hatano, T., Motoi, Y., Abe, O., Shimoji, K., Kamiya, K., Suzuki, M., Hori, M., Yoshida, M., Hattori, N., Aoki, S., 2014. A preliminary diffusional kurtosis imaging study of Parkinson disease: comparison with conventional diffusion tensor imaging. Neuroradiology 56, 251–258. doi:10.1007/s00234-014-1327-1.

Kamagata, K., Tomiyama, H., Motoi, Y., Kano, M., Abe, O., Ito, K., Shimoji, K., Suzuki, M., Hori, M., Nakanishi, A., Kuwatsuru, R., Sasai, K., Aoki, S., Hattori, N., 2013. Diffusional kurtosis imaging of cingulate fibers in Parkinson disease: comparison with conventional diffusion tensor imaging. Magn. Reson. Imaging 31, 1501–1506. doi:10.1016/J.MRI.2013.06.009.

Kamiya, K., Kamagata, K., Ogaki, K., Hatano, T., Ogawa, T., Takeshige-Amano, H., Murata, S., Andica, C., Murata, K., Feiweier, T., Hori, M., Hattori, N., Aoki, S., 2020. Brain white-matter degeneration due to aging and parkinson disease as revealed by double diffusion encoding. Front. Neurosci. 14, 1–15. doi:10.3389/fnins.2020.584510.

Kellner, E., Dhital, B., Kiselev, V.G., Reisert, M., 2016. Gibbs-ringing artifact removal based on local subvoxel-shifts. Magn. Reson. Med. 76, 1574–1581. doi:10.1002/mrm.26054.

Kerkelä, L., Henriques, R.N., Hall, M.G., Clark, C.A., Shemesh, N., 2019. Validation and noise robustness assessment of microscopic anisotropy estimation with clinically feasible double diffusion encoding MRI. Magn. Reson. Med. doi:10.1002/mrm.28048.

Koch, M.A., Finsterbusch, J., 2008. Compartment size estimation with double wave vector diffusion-weighted imaging. Magn. Reson. Med. 60, 90–101. doi:10.1002/mrm.21514.

Komlosh, M.E., Horkay, F., Freidlin, R.Z., Nevo, U., Assaf, Y., Basser, P.J., 2007. Detection of microscopic anisotropy in gray matter and in a novel tissue phantom using double pulsed gradient spin echo MR. J. Magn. Reson. 189, 38–45. doi:10.1016/J.JMR.2007.07.003.

Komlosh, M.E., Lizak, M.J., Horkay, F., Freidlin, R.Z., Basser, P.J., 2008. Observation of microscopic diffusion anisotropy in the spinal cord using double-pulsed gradient spin echo MRI. Magn. Reson. Med. 59, 803–809. doi:10.1002/mrm.21528.

Kunz, N., Sizonenko, S.V., Hüppi, P.S., Gruetter, R., Van de Looij, Y., 2013. Investigation of field and diffusion time dependence of the diffusion-weighted signal at ultrahigh magnetic fields. NMR Biomed. 26, 1251–1257. doi:10.1002/nbm.2945.

Lampinen, B., Szczepankiewicz, F., Mårtensson, J., van Westen, D., Sundgren, P.C., Nilsson, M., 2017. Neurite density imaging *versus* imaging of microscopic anisotropy in diffusion MRI: a model comparison using spherical tensor encoding. Neuroimage 147, 517–531. doi:10.1016/j.neuroimage.2016.11.053.

Lampinen, B., Szczepankiewicz, F., Novén, M., van Westen, D., Hansson, O., Englund, E., Mårtensson, J., Westin, C.F., Nilsson, M., 2019. Searching for the neurite density with diffusion MRI: challenges for biophysical modeling. Hum. Brain Mapp. 40, 2529–2545. doi:10.1002/hbm.24542.

Lampinen, B., Szczepankiewicz, F., Mårtensson, J., van Westen, D., Hansson, O., Westin, C.F., Nilsson, M., 2020a. Towards unconstrained compartment modeling in white matter using diffusion-relaxation MRI with tensor-valued diffusion encoding. Magn. Reson. Med. 84, 1605–1623. doi:10.1002/mrm.28216.

Lampinen, B., Zampeli, A., Björkman-Burtscher, I.M., Szczepankiewicz, F., Källén, K., Compagno Strandberg, M., Nilsson, M., 2020b. Tensor-valued diffusion MRI differentiates cortex and white matter in malformations of cortical development associated with epilepsy. Epilepsia 61, 1701–1713. doi:10.1111/epi.16605.

Lasič, S., Szczepankiewicz, F., Eriksson, S., Nilsson, M., Topgaard, D., 2014. Microanisotropy imaging: quantification of microscopic diffusion anisotropy and orientation of order parameter by diffusion MRI with magic-angle spinning of the q-vectorâ€. Front. Phys. 2, 1–14. doi:10.3389/fphy.2014.00028.

Lawrenz, M., Brassen, S., Finsterbusch, J., 2016. Microscopic diffusion anisotropy in the human brain: age-related changes. Neuroimage 141, 313–325. doi:10.1016/J.NEUROIMAGE.2016.07.031.

Lawrenz, M., Finsterbusch, J., 2019. Detection of microscopic diffusion anisotropy in human cortical gray matter *in vivo* with double diffusion encoding. Magn. Reson. Med. 81, 1296–1306. doi:10.1002/mrm.27451.

Lawrenz, M., Finsterbusch, J., 2015. Mapping measures of microscopic diffusion anisotropy in human brain white matter *in vivo* with double-wave-vector diffusion-weighted imaging. Magn. Reson. Med. 73, 773–783. doi:10.1002/mrm.25140.

Lawrenz, M., Finsterbusch, J., 2013. Double-wave-vector diffusion-weighted imaging reveals microscopic diffusion anisotropy in the living human brain. Magn. Reson. Med. 1082, 1072–1082. doi:10.1002/mrm.24347.

Lawrenz, M., Finsterbusch, J., 2011. Detection of microscopic diffusion anisotropy on a whole-body MR system with double wave vector imaging. Magn. Reson. Med. 66, 1405–1415. doi:10.1002/mrm.22934.

Lawrenz, M., Koch, M.A., Finsterbusch, J., 2010. A tensor model and measures of microscopic anisotropy for double-wave-vector diffusion-weighting experiments with long mixing times. J. Magn. Reson. 202, 43–56. doi:10.1016/j.jmr.2009.09.015.

Le Bihan, D., Breton, E., Lallemand, D., Grenier, P., Cabanis, E., Laval-Jeantet, M., 1986. MR imaging of intravoxel incoherent motions: application to diffusion and perfusion in neurologic disorders. Radiology 161, 401–407. doi:10.1148/radiology.161.2.3763909.

Lee, H.H., Yaros, K., Veraart, J., Pathan, J.L., Liang, F.X., Kim, S.G., Novikov, D.S., Fieremans, E., 2019. Along-axon diameter variation and axonal orientation dispersion revealed with 3D electron microscopy: implications for quantifying brain white matter microstructure with histology and diffusion MRI. Brain Struct. Funct. 224, 1469–1488. doi:10.1007/s00429-019-01844-6.

Lee, H.H., Jespersen, S.N., Fieremans, E., Novikov, D.S., 2020c. The impact of realistic axonal shape on axon diameter estimation using diffusion MRI. Neuroimage 117228. doi:10.1016/j.neuroimage.2020.117228.

Lee, H.H., Papaioannou, A., Novikov, D.S., Fieremans, E., 2020a. *In vivo* observation and biophysical interpretation of time-dependent diffusion in human cortical gray matter. Neuroimage 222, 117054. doi:10.1016/j.neuroimage.2020.117054.

Lee, H.H., Fieremans, E., Novikov, D.S., 2018. What dominates the time dependence of diffusion transverse to axons: intra- or extra-axonal water? Neuroimage 182, 500–510. doi:10.1016/j.neuroimage.2017.12.038.

Lee, H.H., Papaioannou, A., Kim, S.L., Novikov, D.S., Fieremans, E., 2020b. A time-dependent diffusion MRI signature of axon caliber variations and beading. Commun. Biol. 3. doi:10.1038/s42003-020-1050-x.

Leemans, A., Jeurissen, B., Sijbers, J., Jones, D.K., 2009. ExploreDTI: a graphical toolbox for processing, analyzing, and visualizing diffusion MR data. Proc. Int. Soc. Magn. Reson. Med. 17, 3537.

Lin, L., Bhawana, R., Xue, Y., Duan, Q., Jiang, R., Chen, H., Chen, X., Sun, B., Lin, H., 2018. Comparative analysis of diffusional kurtosis imaging, diffusion tensor imaging, and diffusion-weighted imaging in grading and assessing cellular proliferation of meningiomas. Am. J. Neuroradiol. 39, 1032–1038. doi:10.3174/ajnr.A5662.

Lu, H., Jensen, J.H., Ramani, A., Helpern, J.A., 2006. Three-dimensional characterization of non-gaussian water diffusion in humans using diffusion kurtosis imaging. NMR Biomed. 19, 236–247. doi:10.1002/nbm.1020.

Lundell, H., Najac, C., Bulk, M., Kan, H.E., Webb, A.G., Ronen, I., 2021. Compartmental diffusion and microstructural properties of human brain gray and white matter studied with double diffusion encoding magnetic resonance spectroscopy of metabolites and water. Neuroimage 234, 117981. doi:10.1016/j.neuroimage.2021.117981.

McNab, J.A., Polimeni, J.R., Wang, R., Augustinack, J.C., Fujimoto, K., Stevens, A., Janssens, T., Farivar, R., Folkerth, R.D., Vanduffel, W., Wald, L.L., 2013a. Surface based analysis of diffusion orientation for identifying architectonic domains in the *in vivo* human cortex. Neuroimage 69, 87–100. doi:10.1016/J.NEUROIMAGE.2012.11.065.

McNab, J.A., Edlow, B.L., Witzel, T., Huang, S.Y., Bhat, H., Heberlein, K., Feiweier, T., Liu, K., Keil, B., Cohen-Adad, J., Tisdall, M.D., Folkerth, R.D., Kinney, H.C., Wald, L.L., 2013b. The human connectome project and beyond: initial applications of 300mT/m gradients. Neuroimage 80, 234–245. doi:10.1016/j.neuroimage.2013.05.074.

Mills, R., 1973. Self-diffusion in normal and heavy water in the range 1–45°. J. Phys. Chem. 77 (5), 685–688. doi:10.1021/j100624a025.

Mitra, P.P., 1995. Multiple wave-vector extensions of the NMR pulsed-field-gradient spin-echo diffusion measurement. Phys. Rev. B 51, 74–78. doi:10.1103/PhysRevB.51.15074.

Mohammadi, S., Tabelow, K., Ruthotto, L., Feiweier, T., Polzehl, J., Weiskopf, N., 2015. High-resolution diffusion kurtosis imaging at 3T enabled by advanced post-processing. Front. Neurosci. 9, 427. doi:10.3389/fnins.2014.00427.

Moseley, M.E., Cohen, Y., Mintorovitch, J., Chileuitt, L., Shimizu, H., Kucharczyk, J., Wendland, M.F., Weinstein, P.R., 1990. Early detection of regional cerebral ischemia in cats: comparison of diffusion- and T2-weighted MRI and spectroscopy. Magn. Reson. Med. 14, 330–346. doi:10.1002/mrm.1910140218.

Mueller, L., Wetscherek, A., Kuder, T.A., Laun, F.B., 2017. Eddy current compensated double diffusion encoded (DDE) MRI. Magn. Reson. Med. 77, 328–335. doi:10.1002/mrm.26092.

Mukherjee, P., 2005. Diffusion tensor imaging and fiber tractography in acute stroke. Neuroimaging Clin. N. Am. 15, 655–665. doi:10.1016/j.nic.2005.08.010.

Mulkern, R.V., Gudbjartsson, H., Westin, C.F., Zengingonul, H.P., Gartner, W., Guttmann, C.R.G., Robertson, R.L., Kyriakos, W., Schwartz, R., Holtzman, D., Jolesz, F.A., Maier, S.E., 1999. Multi-component apparent diffusion coefficients in human brain. NMR Biomed. 12, 51–62 10.1002/(SICI)1099-1492(199902)12:1<51::AID-NBM546>3.0.CO;2-E.

Neeman, M., Freyer, J.P., Sillerud, L.O., 1991. A simple method for obtaining cross-term-free images for diffusion anisotropy studies in NMR microimaging. Magn. Reson. Med. 21, 138–143. doi:10.1002/mrm.1910210117.

Nilsson, M., Lasič, S., Drobnjak, I., Topgaard, D., Westin, C.F., 2017. Resolution limit of cylinder diameter estimation by diffusion MRI: the impact of gradient waveform and orientation dispersion. NMR Biomed. 30, 1–13. doi:10.1002/nbm.3711.

Nilsson, M., Lätt, J., Nordh, E., Wirestam, R., Ståhlberg, F., Brockstedt, S., 2009. On the effects of a varied diffusion time in vivo: is the diffusion in white matter restricted? Magn. Reson. Imaging 27, 176–187. doi:10.1016/J.MRI.2008.06.003.

Nilsson, M., Lätt, J., Van Westen, D., Brockstedt, S., Lasič, S., Ståhlberg, F., Topgaard, D., 2013. Noninvasive mapping of water diffusional exchange in the human brain using filter-exchange imaging. Magn. Reson. Med. 69, 1572–1580. doi:10.1002/mrm.24395.

Nilsson, M., Szczepankiewicz, F., Brabec, J., Taylor, M., Westin, C.F., Golby, A., van Westen, D., Sundgren, P.C., 2020. Tensor-valued diffusion MRI in under 3 min: an initial survey of microscopic anisotropy and tissue heterogeneity in intracranial tumors. Magn. Reson. Med. 83, 608–620. doi:10.1002/mrm.27959.

Ning, L., Nilsson, M., Lasic, S., Westin, C.F., Rathi, Y., 2018. Cumulant expansions for measuring water exchange using diffusion MRI. J. Chem. Phys. 148, 074109. doi:10.1063/1.5014044.

Novikov, D.S., 2021. The present and the future of microstructure MRI: from a paradigm shift to normal science. J. Neurosci. Methods 351, 108947. doi:10.1016/j.jneumeth.2020.108947.

Novikov, D.S., Fieremans, E., Jespersen, S.N., Kiselev, V.G., 2019. Quantifying brain microstructure with diffusion MRI: theory and parameter estimation. NMR Biomed. 32, 1–53. doi:10.1002/nbm.3998.

Novikov, D.S., Jensen, J.H., Helpern, J.A., Fieremans, E., 2014. Revealing mesoscopic structural universality with diffusion. Proc. Natl. Acad. Sci. U. S. A. 111, 5088–5093. doi:10.1073/pnas.1316944111.

Novikov, D.S., Kiselev, V.G., Jespersen, S.N., 2018. On modeling. Magn. Reson. Med. 79, 3172–3193. doi:10.1002/mrm.27101.

Olesen, J.L., Østergaard, L., Shemesh, N., Jespersen, S.N., 2022. Diffusion time dependence, power-law scaling, and exchange in gray matter. Neuroimage doi:10.1016/j.neuroimage.2022.118976, (In press).

Özarslan, E., 2009. Compartment shape anisotropy (CSA) revealed by double pulsed field gradient MR. J. Magn. Reson. 199, 56–67. doi:10.1016/J.JMR.2009.04.002.

Özarslan, E., Basser, P.J., 2008. Microscopic anisotropy revealed by NMR double pulsed field gradient experiments with arbitrary timing parameters. J. Chem. Phys. 128. doi:10.1063/1.2905765.

Palombo, M., Ligneul, C., Hernandez-Garzon, E., Valette, J., 2018. Can we detect the effect of spines and leaflets on the diffusion of brain intracellular metabolites? Neuroimage 182, 283–293. doi:10.1016/j.neuroimage.2017.05.003.

Paulsen, J.L., Özarslan, E., Komlosh, M.E., Basser, P.J., Song, Y.Q., 2015. Detecting compartmental non-Gaussian diffusion with symmetrized double-PFG MRI. NMR Biomed. 28, 1550–1556. doi:10.1002/nbm.3363.

Percheron, G., Yelnik, J., François, C., 1984. A Golgi analysis of the primate globus pallidus. III. Spatial organization of the striato-pallidal complex. J. Comp. Neurol. 227, 214–227. doi:10.1002/cne.902270207.

Portnoy, S., Flint, J.J., Blackband, S.J., Stanisz, G.J., 2013. Oscillating and pulsed gradient diffusion magnetic resonance microscopy over an extended b-value range: implications for the characterization of tissue microstructure. Magn. Reson. Med. 69, 1131–1145. doi:10.1002/mrm.24325.

Raab, P., Hattingen, E., Franz, K., Zanella, F.E., 2010. Cerebral gliomas: diffusional kurtosis imaging analysis of microstructural differences. Radiology 254, 876–881.

Raja, R., Sinha, N., Saini, J., Mahadevan, A., Rao, K.N., Swaminathan, A., 2016. Assessment of tissue heterogeneity using diffusion tensor and diffusion kurtosis imaging for grading gliomas. Neuroradiology 58, 1217–1231. doi:10.1007/s00234-016-1758-y.

Roebroeck, A., Galuske, R., Formisano, E., Chiry, O., Bratzke, H., Ronen, I., Kim, D., shik, Goebel, R., 2008. High-resolution diffusion tensor imaging and tractography of the human optic chiasm at 9.4 T. Neuroimage 39, 157–168. doi:10.1016/j.neuroimage.2007.08.015.

Scholz, J., Klein, M.C., Behrens, T.E.J., Johansen-Berg, H., 2009. Training induces changes in white-matter architecture. Nat. Neurosci. 12, 1370–1371. doi:10.1038/nn.2412.

Shemesh, N., 2018. Axon diameters and myelin content modulate microscopic fractional anisotropy at short diffusion times in fixed rat spinal cord. Front. Phys. 6, 1–15. doi:10.3389/fphy.2018.00049.

Shemesh, N., Adiri, T., Cohen, Y., 2011. Probing microscopic architecture of opaque heterogeneous systems using double-pulsed-field-gradient NMR. J. Am. Chem. Soc. 133, 6028–6035. doi:10.1021/ja200303h.

Shemesh, N., Barazany, D., Sadan, O., Bar, L., Zur, Y., Barhum, Y., Sochen, N., Offen, D., Assaf, Y., Cohen, Y., 2012b. Mapping apparent eccentricity and residual ensemble anisotropy in the gray matter using angular double-pulsed-field-gradient MRI. Magn. Reson. Med. 68, 794–806. doi:10.1002/mrm.23300.

Shemesh, N., Cohen, Y., 2011. Microscopic and compartment shape anisotropies in gray and white matter revealed by angular bipolar double-PFG MR. Magn. Reson. Med. 65, 1216–1227. doi:10.1002/mrm.22738.

Shemesh, N., Jespersen, S.N., Alexander, D.C., Cohen, Y., Drobnjak, I., Dyrby, T.B., Finsterbusch, J., Koch, M.A., Kuder, T., Laun, F., Lawrenz, M., Lundell, H., Mitra, P.P., Nilsson, M., Özarslan, E., Topgaard, D., Westin, C.F., 2016. Conventions and nomenclature for double diffusion encoding NMR and MRI. Magn. Reson. Med. 75, 82–87. doi:10.1002/mrm.25901.

Shemesh, N., Özarslan, E., Adiri, T., Basser, P.J., Cohen, Y., 2010b. Noninvasive bipolar double-pulsed-field-gradient NMR reveals signatures for pore size and shape in polydisperse, randomly oriented, inhomogeneous porous media. J. Chem. Phys. 133. doi:10.1063/1.3454131.

Shemesh, N., Özarslan, E., Basser, P.J., Cohen, Y., 2012a. Accurate noninvasive measurement of cell size and compartment shape anisotropy in yeast cells using double-pulsed field gradient MR. NMR Biomed. 25, 236–246. doi:10.1002/nbm.1737.

Shemesh, N., Özarslan, E., Komlosh, M.E., Basser, P.J., Cohen, Y., 2010a. From single-pulsed field gradient to double-pulsed field gradient MR: gleaning new microstructural information and developing new forms of contrast in MRI. NMR Biomed. 23, 757–780. doi:10.1002/nbm.1550.

Shemesh, N., Rosenberg, J.T., Dumez, J.N., Grant, S.C., Frydman, L., 2017. Distinguishing neuronal from astrocytic subcellular microstructures using *in vivo* double diffusion encoded 1H MRS at 21.1 T. PLoS One 12, 1–19. doi:10.1371/journal.pone.0185232.

Shemesh, N., Rosenberg, J.T., Dumez, J.N., Muniz, J.A., Grant, S.C., Frydman, L., 2014. Metabolic properties in stroked rats revealed by relaxation-enhanced magnetic resonance spectroscopy at ultrahigh fields. Nat. Commun. 5, 1–8. doi:10.1038/ncomms5958.

Skinner, N.P., Kurpad, S.N., Schmit, B.D., Budde, M.D., 2015. Detection of acute nervous system injury with advanced diffusion-weighted MRI: a simulation and sensitivity analysis. NMR Biomed. 28, 1489–1506. doi:10.1002/nbm.3405.

Stejskal, E.O., Tanner, J.E., 1965. Spin diffusion measurements: spin echoes in the presence of a time-dependent field gradient. J. Chem. Phys. 42, 288–292. doi:10.1192/bjp.111.479.1009-a.

Steven, A.J., Zhuo, J., Melhem, E.R., 2014. Diffusion kurtosis imaging: an emerging technique for evaluating the microstructural environment of the brain. Am. J. Roentgenol. 202, 26–33. doi:10.2214/AJR.13.11365.

Struyfs, H., Van Hecke, W., Veraart, J., Sijbers, J., Slaets, S., De Belder, M., Wuyts, L., Peters, B., Sleegers, K., Robberecht, C., Van Broeckhoven, C., De Belder, F., Parizel, P.M., Engelborghs, S., 2015. Diffusion kurtosis imaging: a possible MRI biomarker for AD diagnosis? J. Alzheimer's Dis. 48, 937–948. doi:10.3233/JAD-150253.

Surova, Y., Nilsson, M., Lampinen, B., Lätt, J., Hall, S., Widner, H., van Westen, D., Hansson, O., 2018. Alteration of putaminal fractional anisotropy in Parkinson's disease: a longitudinal diffusion kurtosis imaging study. Neuroradiology 60, 247–254. doi:10.1007/s00234-017-1971-3.

Szczepankiewicz, F., Lasič, S., van Westen, D., Sundgren, P.C., Englund, E., Westin, C.F., Ståhlberg, F., Lätt, J., Topgaard, D., Nilsson, M., 2015. Quantification of microscopic diffusion anisotropy disentangles effects of orientation dispersion from microstructure: applications in healthy volunteers and in brain tumors. Neuroimage 104, 241–252. doi:10.1016/j.neuroimage.2014.09.057.

Szczepankiewicz, F., Sjölund, J., Ståhlberg, F., Lätt, J., Nilsson, M., 2019a. Tensor-valued diffusion encoding for diffusional variance decomposition (DIVIDE): technical feasibility in clinical MRI systems. PLoS One 14, 1–20. doi:10.1371/journal.pone.0214238.

Szczepankiewicz, F., van Westen, D., Englund, E., Westin, C.F., Ståhlberg, F., Lätt, J., Sundgren, P.C., Nilsson, M., 2016. The link between diffusion MRI and tumor heterogeneity: mapping cell eccentricity and density by diffusional variance decomposition (DIVIDE). Neuroimage 142, 522–532. doi:10.1016/j.neuroimage.2016.07.038.

Szczepankiewicz, F., Lasic, S., Nilsson, M., Lundell, H., Westin, C., Topgaard, D., 2019b. Is spherical diffusion encoding rotation invariant? An investigation of diffusion time-dependence in the healthy brain. In: Proceedings of the International Society for Magnetic Resonance in Medicine, p. 0223.

Szczepankiewicz, F., Westin, C., Nilsson, M., 2019c. Maxwell-compensated design of asymmetric gradient waveforms for tensor-valued diffusion encoding. Magn. Reson. Med. Sci. 82, 1424–1437. doi:10.1002/mrm.27828.

Szczepankiewicz, F., Westin, C.F., Nilsson, M., 2021. Gradient waveform design for tensor-valued encoding in diffusion MRI. J. Neurosci. Methods 348, 109007. doi:10.1016/j.jneumeth.2020.109007.

Tabesh, A., Jensen, J.H., Ardekani, B.A., Helpern, J.A., 2011. Estimation of tensors and tensor-derived measures in diffusional kurtosis imaging. Magn. Reson. Med. 65, 823–836. doi:10.1002/mrm.22655.

Tax, C.M.W., Szczepankiewicz, F., Nilsson, M., Jones, D.K., 2020. The dot-compartment revealed? Diffusion MRI with ultra-strong gradients and spherical tensor encoding in the living human brain. Neuroimage 210, 116534. doi:10.1016/j.neuroimage.2020.116534.

Topgaard, D., 2019. Diffusion tensor distribution imaging. NMR Biomed. 32, 1–12. doi:10.1002/nbm.4066.

Topgaard, D., 2017. Multidimensional diffusion MRI. J. Magn. Reson. 275, 98–113. doi:10.1016/j.jmr.2016.12.007.

Tournier, J.D., Smith, R., Raffelt, D., Tabbara, R., Dhollander, T., Pietsch, M., Christiaens, D., Jeurissen, B., Yeh, C.H., Connelly, A., 2019. MRtrix3: a fast, flexible and open software framework for medical image processing and visualisation. Neuroimage 202, 116137. doi:10.1016/j.neuroimage.2019.116137.

Tustison, N.J., Avants, B.B., Cook, P.A., Zheng, Y., Egan, A., Yushkevich, P.A., Gee, J.C., 2010. N4ITK: improved N3 bias correction. IEEE Trans. Med. Imaging 29, 1310–1320. doi:10.1109/TMI.2010.2046908.

Van, A.T., Holdsworth, S.J., Bammer, R., 2014. *In vivo* investigation of restricted diffusion in the human brain with optimized oscillating diffusion gradient encoding. Magn. Reson. Med. 71. doi:10.1021/nn300902w.Release.

van der Kouwe, A.J.W., Benner, T., Salat, D.H., Fischl, B., 2008. Brain morphometry with multiecho MPRAGE. Neuroimage 40, 559–569. doi:10.1016/j.neuroimage.2007.12.025.

Veraart, J., Novikov, D.S., Christiaens, D., Ades-aron, B., Sijbers, J., Fieremans, E., 2016. Denoising of diffusion MRI using random matrix theory. Neuroimage 142, 394–406. doi:10.1016/j.neuroimage.2016.08.016.

Veraart, J., Rajan, J., Peeters, R.R., Leemans, A., Sunaert, S., Sijbers, J., 2013. Comprehensive framework for accurate diffusion MRI parameter estimation. Magn. Reason. Med. 70, 972–984. doi:10.1002/mrm.24529.

Vincent, M., Palombo, M., Valette, J., 2020. Revisiting double diffusion encoding MRS in the mouse brain at 11.7T: which microstructural features are we sensitive to? Neuroimage 207. doi:10.1016/j.neuroimage.2019.116399.

Vos, S.B., Tax, C.M.W., Luijten, P.R., Ourselin, S., Leemans, A., Froeling, M., 2017. The importance of correcting for signal drift in diffusion MRI. Magn. Reson. Med. 77 (1), 285–299. doi:10.1002/mrm.26124.

Wang, J.J., Lin, W.Y., Lu, C.S., Weng, Y.H., Ng, S.H., Wang, C.H., Liu, H.L., Hsieh, R.H., Wan, Y.L., Wai, Y.Y., 2011. Parkinson disease: diagnostic utility of diffusion kurtosis imaging. Radiology 261, 210–217. doi:10.1148/radiol.11102277.

Westin, C.F., Knutsson, H., Pasternak, O., Szczepankiewicz, F., Özarslan, E., van Westen, D., Mattisson, C., Bogren, M., O'Donnell, L.J., Kubicki, M., Topgaard, D., Nilsson, M., 2016. Q-space trajectory imaging for multidimensional diffusion MRI of the human brain. Neuroimage 135, 345–362. doi:10.1016/J.NEUROIMAGE.2016.02.039.

Westin, C.F., Szczepankiewicz, F., Pasternak, O., Özarslan, E., Topgaard, D., Knutsson, H., Nilsson, M., 2014. Measurement tensors in diffusion MRI: generalizing the concept of diffusion encoding. Med. Image Comput. Comput. Assist. Interv. 17 (Pt 3), 209–216. doi:10.1007/978-3-319-10443-0_27.

Winther Andersen, K., Lasič, S., Lundell, H., Nilsson, M., Topgaard, D., Sellebjerg, F., Szczepankiewicz, F., Siebner, H.R., Blinkenberg, M., Dyrby, T.B., 2020. Disentangling white-matter damage from physiological fibre orientation dispersion in multiple sclerosis. Brain Commun. 2. doi:10.1093/braincomms/fcaa077.

Wu, E.X., Cheung, M.M., 2010. MR diffusion kurtosis imaging for neural tissue characterization. NMR Biomed. 23, 836–848. doi:10.1002/nbm.1506.

Yang, G., Tian, Q., Leuze, C., Wintermark, M., McNab, J.A., 2018. Double diffusion encoding MRI for the clinic. Magn. Reson. Med. 80, 507–520. doi:10.1002/mrm.27043.

Yon, M., Bao, Q., Chitrit, O.J., Henriques, R.N., Shemesh, N., Frydman, L., 2020. High-resolution 3D *in vivo* brain diffusion tensor imaging at ultrahigh fields: following maturation on juvenile and adult mice. Front. Neurosci. 14, 1–14. doi:10.3389/fnins.2020.590900.

Zhang, H., Schneider, T., Wheeler-kingshott, C.A., Alexander, D.C., 2012. NODDI : practical *in vivo* neurite orientation dispersion and density imaging of the human brain. Neuroimage 61, 1000–1016. doi:10.1016/j.neuroimage.2012.03.072.

Zhuo, J., Xu, S., Proctor, J.L., Mullins, R.J., Simon, J.Z., Fiskum, G., Gullapalli, R.P., 2012. Diffusion kurtosis as an *in vivo* imaging marker for reactive astrogliosis in traumatic brain injury. Neuroimage 59, 467–477. doi:10.1016/j.neuroimage.2011.07.050.